AN ABSTRACT OF THE THESIS OF

Shu-ching Hsu for the degree of Master of Science in Electrical and Computer Engineering presented on January 12, 2004.

Title: Analysis and Modeling of Substrate Noise Coupling for NMOS Transistors in Heavily Doped Substrates.

Abstract approved:

Redacted for Privacy

Redacted for Privacy

Kartikeya Mayaram

Terri S. Fiez

This thesis examines substrate noise coupling for NMOS transistors in heavily doped substrates. The study begins with the analysis of an NMOS transistor switching noise in a digital inverter at the device level. A resistive substrate network for the NMOS transistor is proposed and verified. Coupling between N+-P+ contacts is compared both qualitatively and quantitatively with simulations. The difference between the N-P and P-P coupling is in the cross-coupling parameter. A new N-P model, which requires only five parameters, is proposed by taking advantage of an exsiting P-P model combined with the concept of a virtual separation. This model has been validated up to 2GHz with Medici simulations. The virtual separation concept has been validated with 2D/3D simulations and measurements from test structures fabricated in a 0.35μm TSMC CMOS heavily doped process. This model is useful when transistor switching noise is the dominant source of substrate noise. Applications of the new N-P model are demonstrated with circuit simulations.

Analysis and Modeling of Substrate Noise Coupling for NMOS Transistors in Heavily Doped Substrates

by

Shu-ching Hsu

A THESIS

submitted to

Oregon State University

in partial fulfillment of
the requirements for the
degree of

Master of Science

Presented January 12, 2004

Commencement June 2004

Master of Science thesis of Shu-ching Hsu presented on January 12, 2004

APPROVED:

Redacted for Privacy

Co-Major Professor, representing Electrical and Computer Engineering

Redacted for Privacy

Co-Major Professor, representing Electrical and Computer Engineering

Redacted for Privacy

Director of the School of Electrical Engineering and Computer Science

Redacted for Privacy

Dean of the Graduate School

I understand that my thesis will become part of the permanent collection of Oregon State University libraries. My signature below authorizes release of my thesis to any reader upon request.

Redacted for Privacy

Shu-ching Hsu, Author

ACKNOWLEDGEMENT

First and foremost, I would like to thank my advisors, Dr. Karti Mayaram and Dr. Terri Fiez, for bringing me into this research since my senior year of undergraduate program at Oregon State University. Their technical guidance and, mostly importantly, continuous encouragement have assisted me to explore my research interests and to accomplish this research project. I would like to thank Dr. Chenggang Xu and Dr. Keith Levien for being my committee members. I would like to thank Dr. Chenggang Xu again for many discussions of my research during the past two years.

I would like to thank SRC (Semiconductor Research Corporation) and the SRC Master's Scholarship Program for sponsoring my research work. I would also like to thank SRC's Graduate Fellowship Program Annual Conference for connecting me with people from industry. As a result I obtained several valuable suggestions and comments that helped my research at OSU.

Many thanks to my colleagues, Sirisha Adluri, James Ayers, Patrick Birrer, Husni Habal, Paul Hutchinson, Brian Owen, Ajit Sharma, and Robert Shreeve for all the help and cooperation on this substrate coupling project. I would also like to thank Robert Batten for all the thoughtful discussions on test structures and instruments. I especially thank Taras Dudar and Volodymyr Kratyuk for their help on completing the test chip. I would like to thank Vivek Sharma, Prasad Talasila, and Manas Behera for reviewing my thesis.

I am thankful for Husni Habal and Amy Luoh for their friendship and support during my undergraduate and graduate study at OSU. I would like to thank Ajit Sharma, Patrick Birrer, and Volodymyr Kratyuk for being such great company during these two years. I am greatly thankful to Cheng-yao Chen for his understanding, support, and care for my life in Corvallis.

I am grateful to my uncle, Wai Yuan Chan, and my aunt, Ying-ying Chan, for taking care of me as their own daughter. They are like my parents in the U.S.

Lastly, I would like to greatly thank my parents, Jun-nan Hsu and Chen-chen Hsu and my sister, Ya-ching Hsu. No words are adequate to express the gratitude I feel for them. It is their unconditional love that gives me the courage to accomplish anything in my life.

TABLE OF CONTENTS

TABLE OF CONTENTS (Continued)

Page

TABLE OF CONTENTS (Continued)

Page

LIST OF FIGURES

LIST OF FIGURES (Continued)

LIST OF FIGURES (Continued)

LIST OF FIGURES (Continued)

LIST OF FIGURES (Continued)

LIST OF FIGURES (Continued)

LIST OF FIGURES (Continued)

LIST OF TABLES

LIST OF TABLES (Continued)

LIST OF APPENDIX TABLES

To my family

Analysis and Modeling of Substrate Noise Coupling for NMOS Transistors in Heavily Doped Substrates

1 INTRODUCTION AND BACKGROUND

Integration of systems-on-a-chip (SoC) has provided several advantages over separate discrete chips including: reduced size, lower power consumption and lower cost. However, one of the disadvantages of SoCs is the noise generated from the digital blocks coupled to the sensitive analog and RF circuitry via the common silicon substrate. This effect is called substrate noise coupling.

Substrate noise coupling is primarily made up of power supply noise and transistor switching noise. When a digital inverter switches from high to low or low to high, both the PMOS and NMOS transistors are turned on for a short period of time. During this time, current flows from the power supply to the ground. This instantaneous current combined with the inductance of the package and power/ground lines causes $L\frac{di}{dt}$ noise injection into the substrate through the P+ substrate taps. This is called supply noise and can be minimized by reducing the package inductance [1] [2]. Transistor switching noise is due to the charging and discharging of the transistor parasitic capacitors and the load capacitor when the inverter output switches between the high and low states. For an NMOS transistor, the switching noise is coupled into the substrate from the N+ diffusion regions. As the transistor size increases, more noise is generated and coupled into the substrate.

Substrate noise from digital circuits propagates to analog or RF circuits sharing the same substrate. As a result, the bulk node voltages for these transistors change. The time-varying substrate voltage alters the transistor threshold voltage resulting in the body effect. Therefore, analog/RF circuit performance is degraded

in the presence of substrate noise. For this reason, substrate noise coupling is an important consideration for integrated systems on a chip.

An important aspect of substrate noise coupling is the modeling of the silicon substrate. Several modeling approaches have been used to characterize the substrate, such as the finite difference method [10] [20], the boundary element method [4] [5] [11] [19], the pre-processed boundary element method [3] and the scalable macro model [6]-[9] [12]-[14]. The scalable macro-model is efficient for substrate network computations and can be used for very large circuit problems. Prior work in scalable macro models in [7] and [12]-[14] has focused on coupling between P+ contacts. The substrate network is derived based on P+ contacts and attached to the transistor bulks for circuit simulations. This approach works well when supply noise is the dominant source of noise. The work presented in [8] uses a 121 pin grid array package with pin parasitic inductances ranging from 4nH to 7nH. The substrate network derived from P+ substrate taps provides accurate simulation results, in this case.

As the package inductance reduces to values below 0.1nH [1] [2], switching noise becomes the dominant source of noise. As an example, flip chip packages have pin parasitic inductances ranging from 0.01nH to 0.1nH. In this case, noise injected from the N+ diffusion regions of an NMOS transistor needs to be understood and modeled accurately.

This thesis focuses on addressing the substrate noise coupling problems in heavily doped substrates when transistor switching noise is important. This work starts out with device level simulations of a simple inverter to examine the noise injection in an NMOS transistor. The substrate current flow lines are used to identify a resistive coupling network for the NMOS transistor. Then, the difference between the coupling of P-P and N-P contacts is examined. A new N-P model is required to properly address the coupling between N+ and P+ contacts. The N-P model is developed based on an existing P-P model using the concept of a larger virtual separation. This model is validated with physical measurements.

Simulations of a three-stage ring oscillator circuit and a structure with multiple contacts are used to demonstrate the difference between the N-P model and the P-P model.

The thesis is organized as follows. In Chapter 2, substrate coupling for NMOS transistors in a digital inverter is analyzed. In Chapter 3, the coupling between N+ and P+ contacts is discussed. A new N-P model is developed by taking advantage of an existing P-P model combined with the concept of a virtual separation in Chapter 4. The measurement results and validations of the model are summarized in Chapter 5. Chapter 6 demonstrates applications of the new N-P model when transistor switching noise dominates. Finally, Chapter 7 concludes this work.

2 ANALYSIS OF SUBSTRATE COUPLING IN NMOS TRANSISTORS

The scalable macro-modeling approach is based on z-parameters [12]-[14]. These z-parameters are dependent on the geometry and spacing between substrate contacts. It is important to properly characterize the contact geometry for transistors in this approach. In [12], it is assumed that the entire NMOS transistor active area defines the size of the contact. This assumption needs to be verified by studying the noise injection from a switching transistor. In this chapter, this verification is done using Medici, a 2D device level simulator [15]. The study begins with an inverter consisting of a single-finger NMOS transistor. Then, it continues with the examination of a two-finger NMOS transistor. Finally, substrate network connections for the NMOS transistor of the inverter are proposed and verified.

2.1 Medici Simulations of a Simple Inverter

Transistor switching noise injection into the substrate can be studied by examining noise current flow lines obtained from simulations of a digital inverter structure in Medici. The inverter structure is shown in Figure 2-1(a). In Figure 2-1(a), PMOSFET transistor switching noise first propagates through the N-well, and then through the N-well capacitor, $C_{N\text{-well}}$, to reach the P+ tap through the p-type substrate. For the NMOSFET, the transistor switching noise propagates to the P+ tap directly through the p-type substrate. The propagation of noise through the substrate can be modeled by a resistive network at low frequencies [3][4]. This network is shown as the substrate network block in Figure 2-1(b). The substrate noise current is measured at the P+ tap.

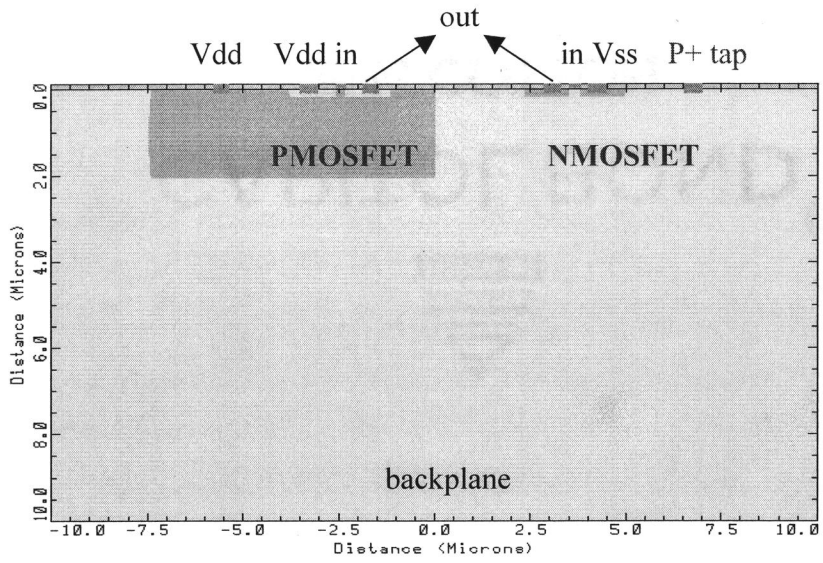

(a)

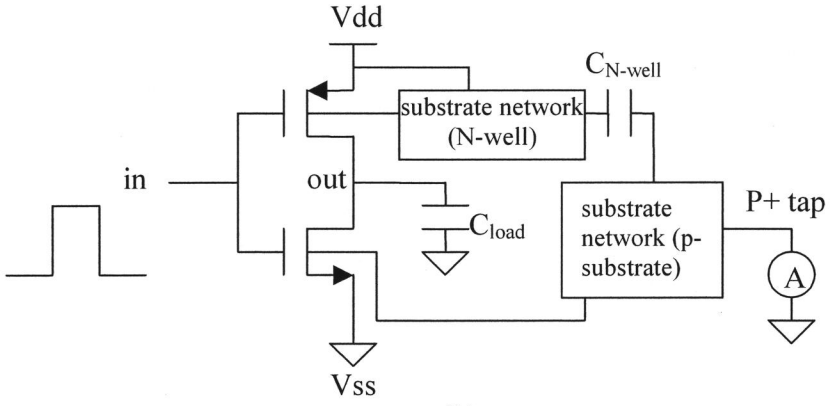

(b)

Figure 2-1 (a) Cross section of the simple inverter structure setup in Medici, and (b) schematic of the simple inverter.

The input of the inverter is clocked at 100MHz. Since the purpose of the study is to examine the noise current flow lines in the substrate when the switching noise is important, the parasitics of the package and the power/ground lines are neglected. The P+ substrate tap next to the NMOS transistor serves as a sensor for the noise current in the substrate. Figure 2-2 shows the simulated waveform of the current through the P+ substrate tap. A negative current peak is sensed when the inverter output switches from high to low and a positive current peak is sensed when the inverter output switches from low to high. This phenomenon is due to the charging and discharging of the parasitic capacitors as explained later.

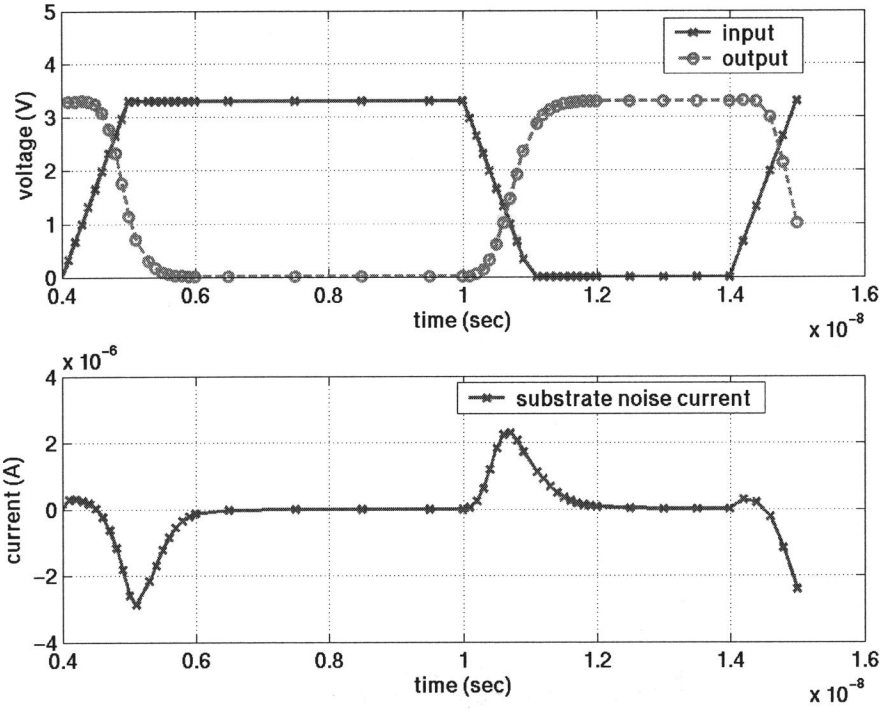

Figure 2-2 Inverter input/output and substrate noise current waveform picked up at the P+ substrate tap adjacent to the NMOS transistor.

The current flow lines are examined at different time instants when the inverter switches between the high and low states as shown in Figure 2-3 and Figure 2-4. The N-well in which the PMOS transistor resides, serves as a barrier to the PMOS transistor noise injection into the substrate. Therefore, there are no current flow lines from the PMOS transistor to the P+ substrate tap. The PMOS transistor noise is picked up by the N+ tap in the N-well as shown in both Figure 2-3 and Figure 2-4. For the NMOS transistor, it is observed that the noise current flows to the P+ substrate tap. An examination of the location of the noise current injection shows that most of the noise current is from the drain region of the transistor.

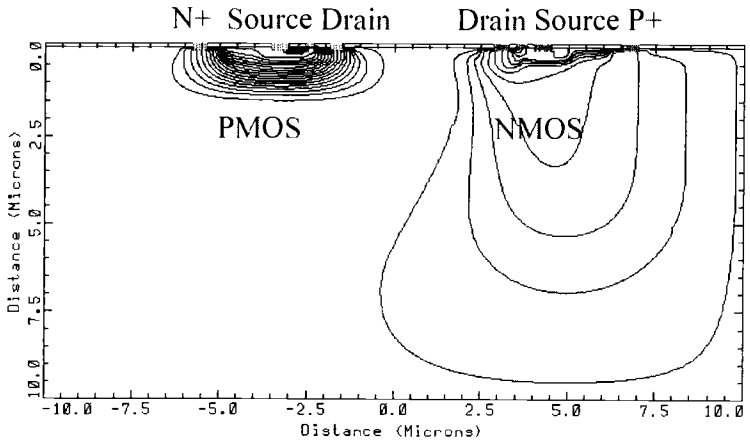

Figure 2-3 Substrate current flow lines at 0.9 ns when the simple inverter output is switching from low to high. The backplane is floating.

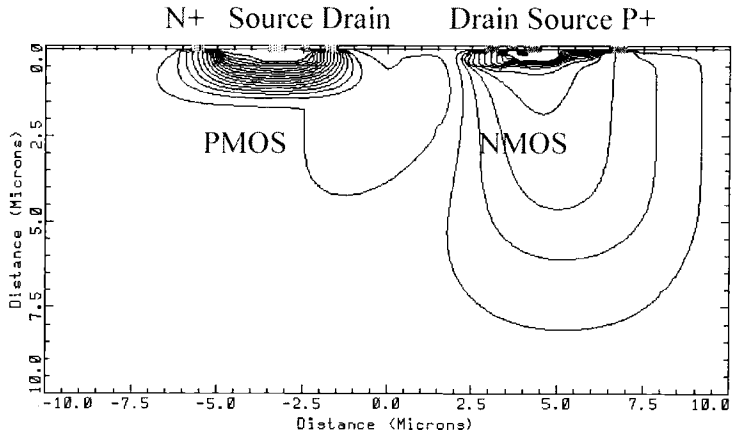

Figure 2-4 Noise current flow lines at 5.1 ns when the simple inverter output is switching from high to low. The backplane is floating.

The substrate noise current generated in this simple inverter is due to the charging and discharging of the drain-bulk capacitor, C_{db} and the off-chip load capacitor, C_{load}. When the simple inverter output switches from low to high, both C_{load} and C_{db} are charged. The path of the charging current is shown in Figure 2-5. When the simple inverter output switches from high to low, both C_{load} and C_{db} are discharged. The path of the discharging current is shown in Figure 2-6. From the charging and discharging paths, it is seen that a positive current peak is sensed when the inverter switches from low to high and a negative current peak is sensed when the inverter switches from high to low.

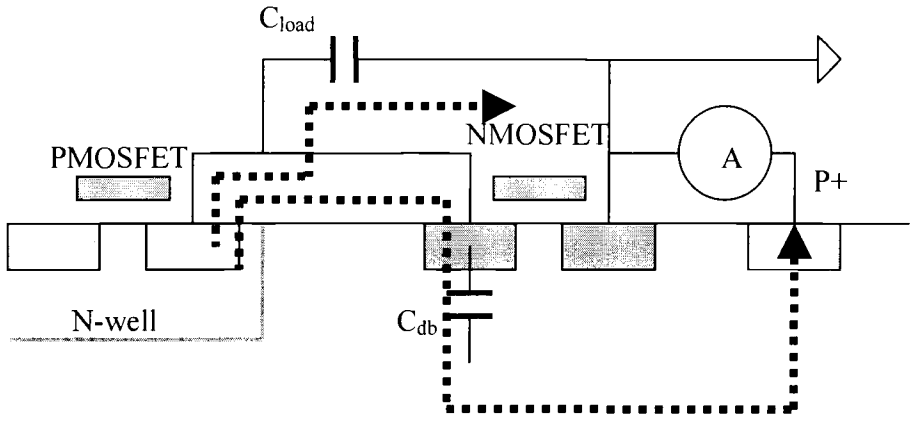

Figure 2-5 Noise current path when the simple inverter output switches from low to high. Both C_{load} and C_{db} are charged. A positive current peak is observed at the P+ substrate tap during this transition. C_{load} is off-chip.

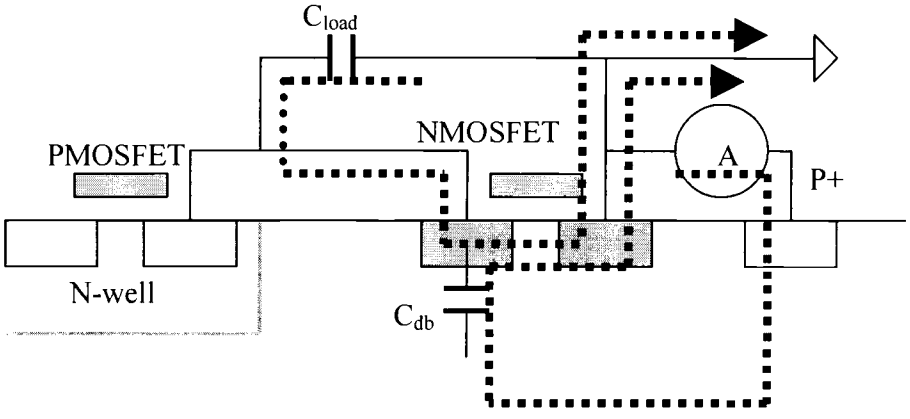

Figure 2-6 Noise current path when the simple inverter output switches from high to low. Both C_{load} and C_{db} are discharged. A negative current peak is observed at the P+ substrate tap during this transition. C_{load} is off-chip.

2.2 Medici Simulations of Two-finger Transistor Structures

In practical circuit layouts, a transistor is laid out as a multi-finger structure to save area and reduce parasitics. In Section 2.1, it is observed that for an inverter, the drain region of the NMOS transistor injects noise into the substrate. Since the PMOS transistor noise injection is within the N-well, the study of the two-finger structures has been focused only on the NMOS transistor drain regions.

2.2.1 Transistor Layout

A double-finger NMOS transistor can be laid out in two variants, either having the source shared, forming the DSD (Drain/Source/Drain) case or having the drain shared, forming the SDS (Source/Drain/Source) case. Both DSD and SDS structures are set up in Medici as shown in Figure 2-7. The PMOS transistor is kept as a single-finger structure for simplicity. Since the study focuses only on transistor switching noise, the power and ground line parasitics are again neglected. The input is clocked at 100 MHz.

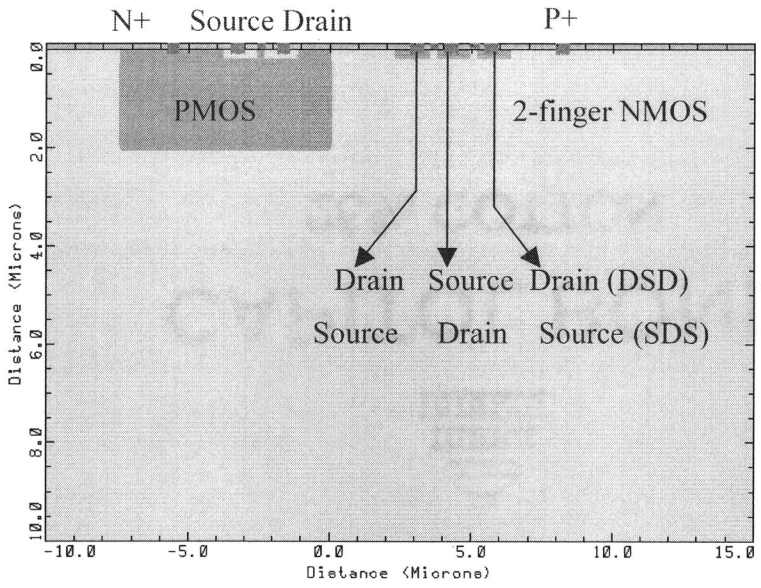

Figure 2-7 Digital inverter cross section with the NMOS transistor as a two-finger structure.

2.2.2 Transistor Noise Injection Results

The noise current flow lines for DSD and SDS layouts during output transitions are shown in Figure 2-8 and Figure 2-9. The PMOS transistor noise injection is within the N-well region as seen in Section 2.1. The noise injection of the NMOS transistor is due to the charging and the discharging of C_{load} and C_{db}. When the inverter output is switching from low to high as shown in Figure 2-8, C_{load} and C_{db} are charged. The charging current of C_{db} flows through the PMOS transistor to the P+ substrate tap. Therefore, a positive noise current peak is observed. When the inverter output switches from high to low as in Figure 2-9, C_{load} and C_{db} are discharged. The discharging current of C_{db} is drawn from the P+ substrate tap. Therefore, a negative noise current peak is seen.

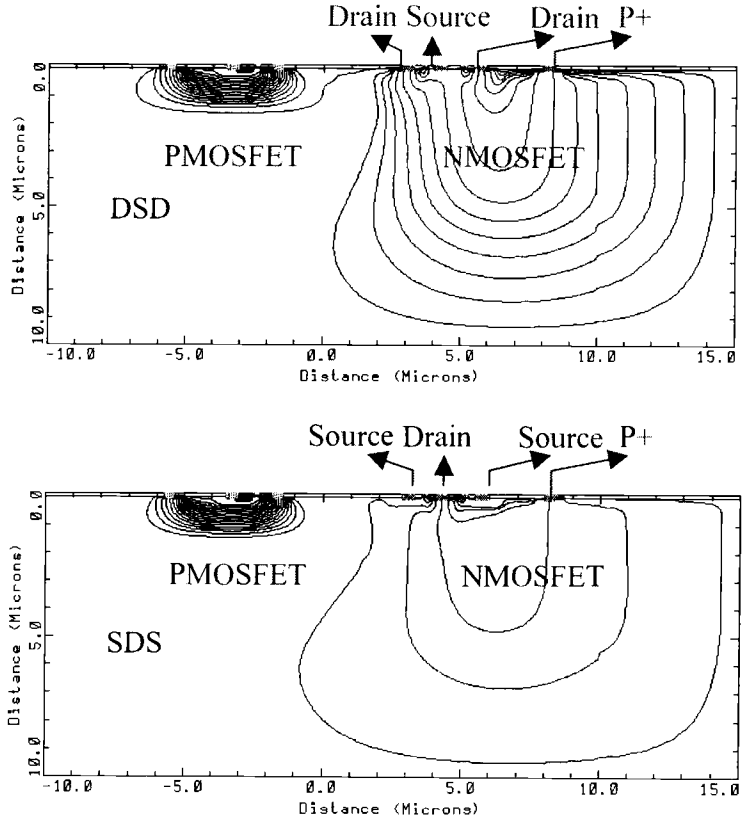

Figure 2-8 Noise current flow lines of inverters with two-finger NMOS transistors at time 1ns when the output is switching from low to high. Most of the noise current is from the drain region of the NMOS transistor.

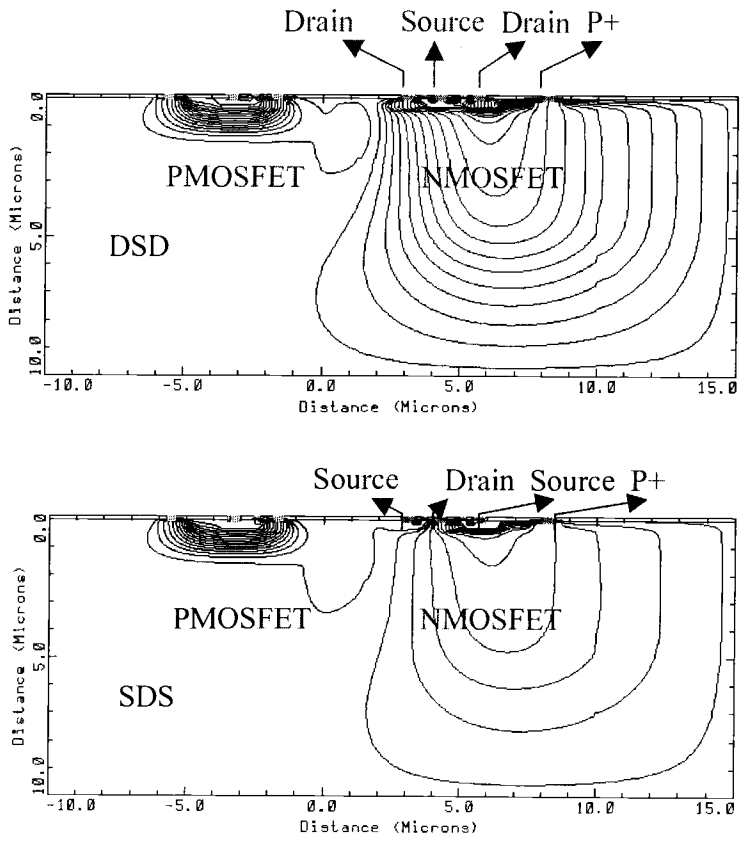

Figure 2-9 Noise current flow lines of inverters with two-finger NMOS transistors at time 5ns when the output is switching from high to low. Most of the noise current is from the drain area of the NMOS transistor.

Figure 2-10 shows the noise current waveform at the P+ substrate tap. From this figure, it can be seen that the P+ substrate tap senses approximately twice the noise current in the DSD case than in the SDS case. The reason for this increase in the noise current is the doubling of C_{db} which is charged or discharged during the switching transitions.

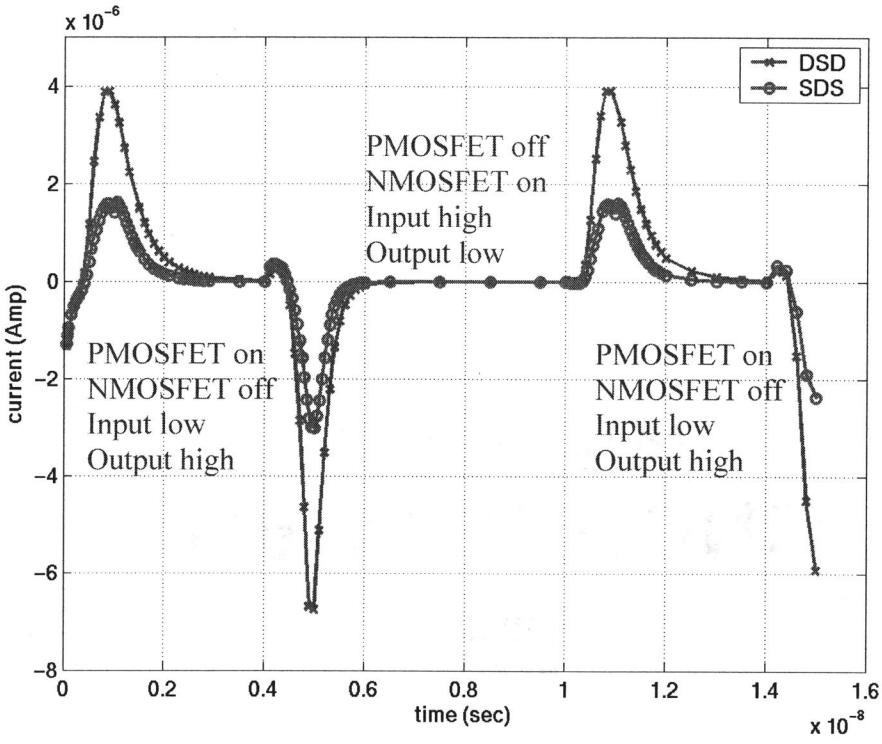

Figure 2-10 Noise current waveform picked up at the P+ substrate tap for DSD and SDS NMOS transistor layouts.

2.2.3 Substrate Network Connection for NMOS Transistor

In Section 2.2.2, the current flow lines in the substrate of an inverter were examined and switching noise injection was explained. From the noise current flow lines, the major noise injection locations were identified. In this section, the current flow lines are used to identify a resistive substrate network that accounts for the coupling through the substrate. Since the PMOS transistor injects little noise into the substrate, its substrate network is ignored.

In Figure 2-11 where a DSD NMOS transistor is shown, the two drain regions and the P+ substrate tap form a substrate resistive network of 3 contacts. Since there is no current flow lines between the two drain regions, the resistance between them is large and can be ignored. For the SDS NMOS transistor in Figure 2-12, the single drain region and the P+ substrate tap form a substrate resistive network of 2 contacts. Figure 2-13 shows the substrate network connections at the circuit level.

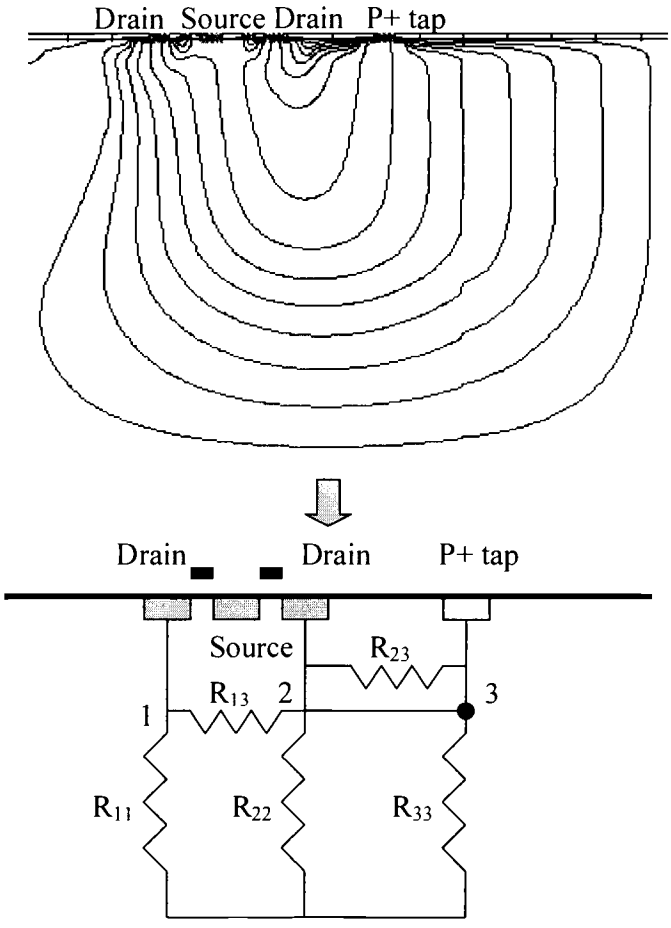

Figure 2-11 Current flow lines used to identify a resistive substrate network for the DSD NMOS transistor.

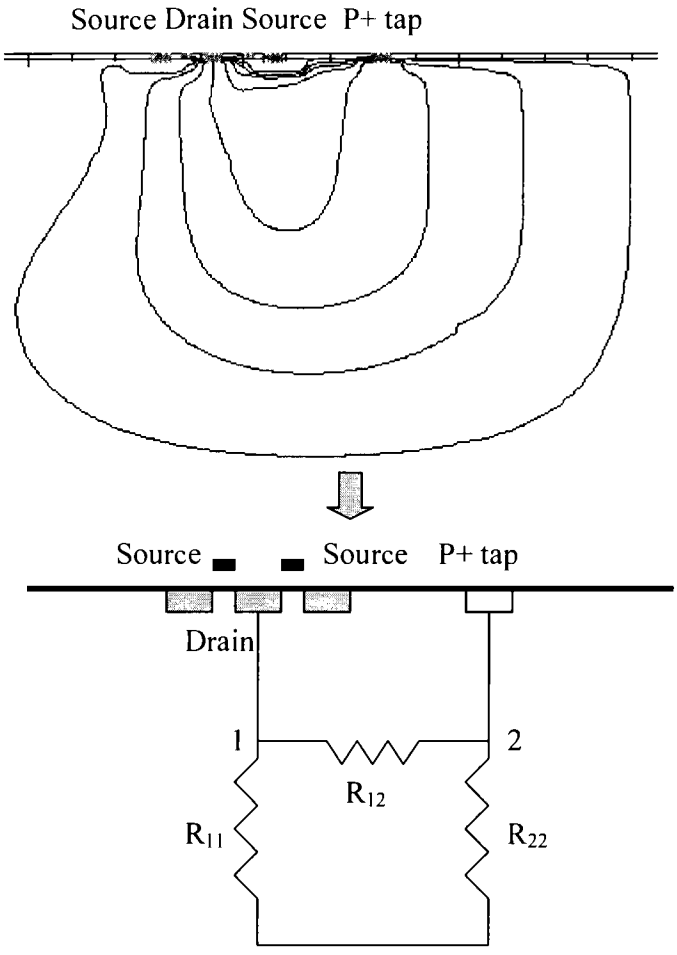

Figure 2-12 Current flow lines used to identify a resistive substrate network for the SDS NMOS transistor.

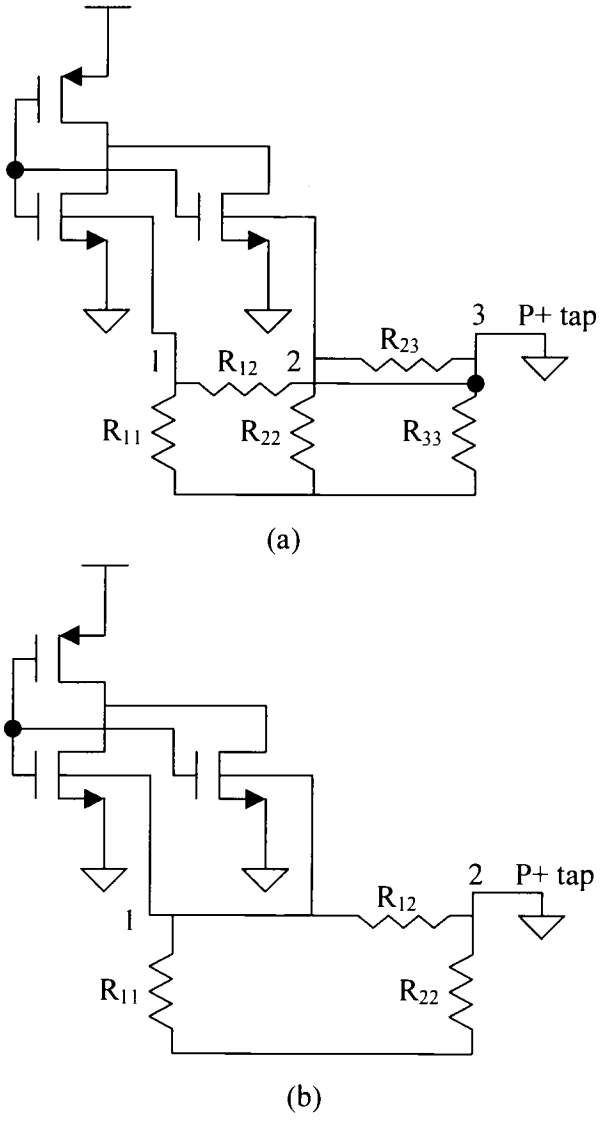

Figure 2-13 Substrate network connections at the circuit level for (a) the DSD, and (b) the SDS NMOS transistors.

From Figure 2-13, it can be seen that the P+ substrate taps and the NMOS transistor bulks, nodes 1 and 2 in Figure 2-13(a) and node 1 in Figure 2-13(b) respectively, are separate nodes. Because of the substrate coupling parasitics, the

transistor bulk nodes are connected to ground via the substrate network. Therefore, the transistor source and bulk are not at the same potential which accounts for the threshold voltage variation due to substrate coupling.

2.2.4 Verification of Substrate Network Connections

In this section, verification of the substrate network for DSD and SDS NMOS transistors is presented. A few modifications to the inverter structures are made.

(1) The PMOS transistor of the inverter is defined by a PMOS transistor model at the circuit level.

(2) The NMOS transistor is defined at the device level and the doping profile for the heavily doped TSMC 0.35μm CMOS process is used.

Two simple experiments, each with DSD and SDS configurations, are conducted here. In the first experiment, the NMOS transistor as the DSD or the SDS structure at the device level, resides in a 10μm-deep substrate with a P+ substrate tap and the substrate noise is examined at the P+ substrate tap. In the second experiment, simulations are done in the mixed device-circuit mode in Medici. The NMOS transistor without the P+ substrate tap resides in a 1μm-deep substrate. The resistances from the transistors to the P+ substrate taps are extracted from the complete NMOS transistor structures in the first experiment and used as resistors at the circuit level in the second experiment. The P+ substrate tap node is now at the circuit level and the noise waveform is examined at this node. Figure 2-14 and Figure 2-15 illustrate the setups in the two experiments.

The purpose of these experiments is to verify the proposed substrate resistive network for the DSD and SDS cases. If noise current sensed from the P+ taps in Figure 2-14(a) is the same as that in 2-14(b), then the resistive network in Figure 2-14(b) accurately models the substrate in Figure 2-14(a). For the SDS case in Figure 2-15, these two experiments are set up for the same reason.

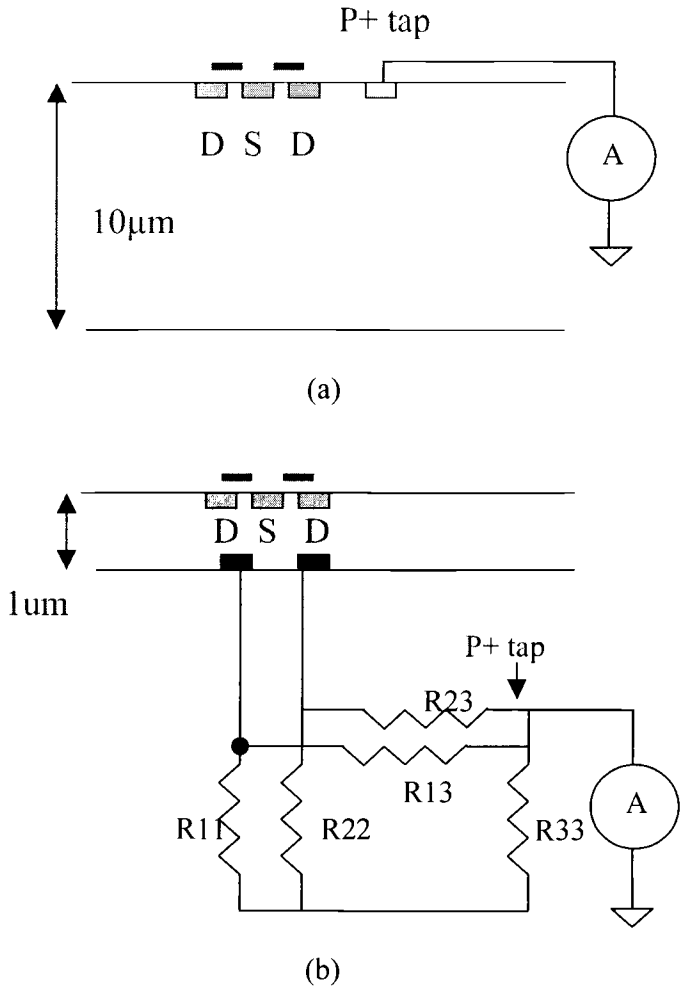

Figure 2-14 (a) A complete DSD NMOS transistor structure with a P+ substrate tap at the device level. (b) A DSD NMOS structure without a P+ substrate tap at the device level and with a resistive substrate network at the circuit level. Resistances are used to model the substrate at the circuit level and are extracted from the complete DSD NMOS structure with the P+ substrate tap.

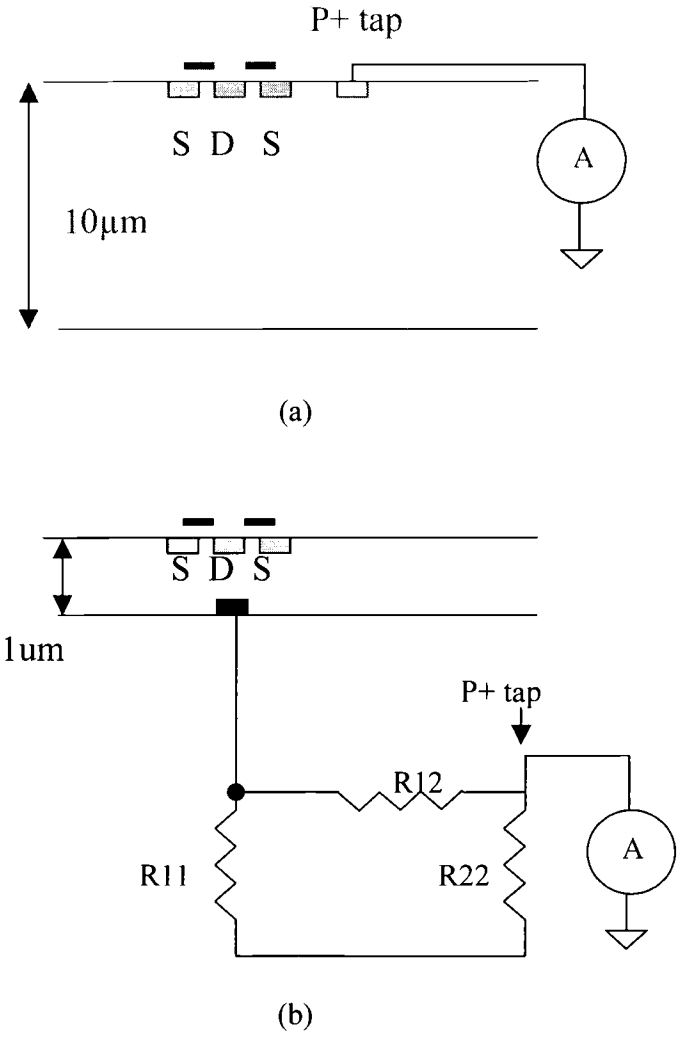

Figure 2-15 (a) A complete SDS NMOS transistor structure with a P+ substrate tap at the device level. (b) A SDS NMOS structure without a P+ substrate tap at the device level and with a resistive substrate network at the circuit level.

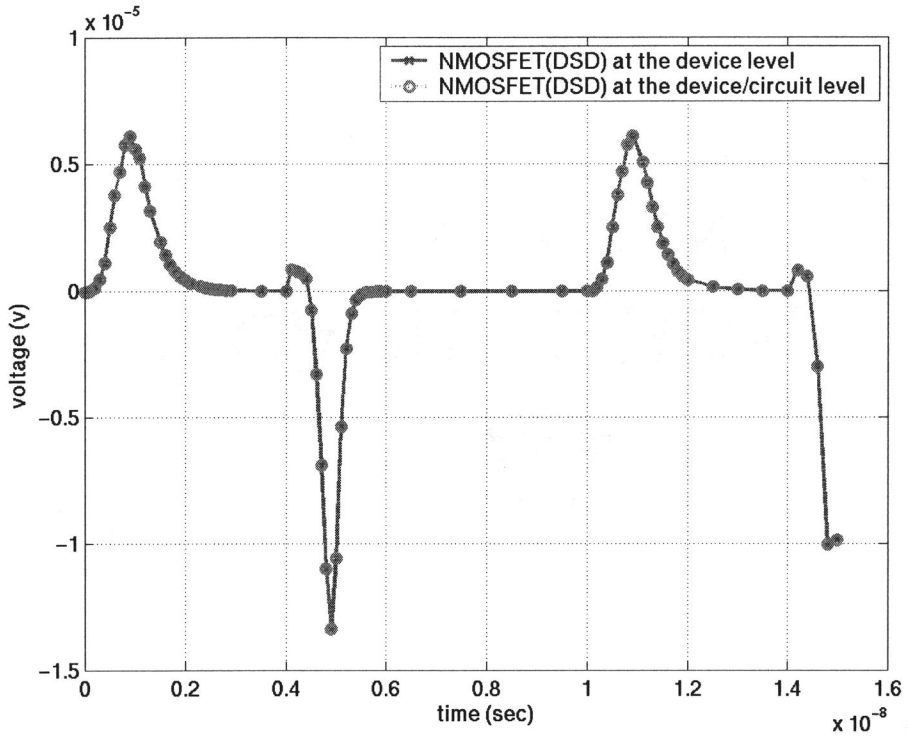

Figure 2-16 Noise waveforms picked up at the P+ substrate tap from the two experiments with DSD NMOS transistors. Simulation results from both experiments agree with each other.

Figure 2-16 shows the noise waveform at the P+ substrate taps both at the device level and at the circuit level with the NMOS transistor as a DSD structure. Both simulations are in close agreement with the pull-up injection peak current magnitude of 6μA and the pull-down injection current peak magnitude of 14μA.

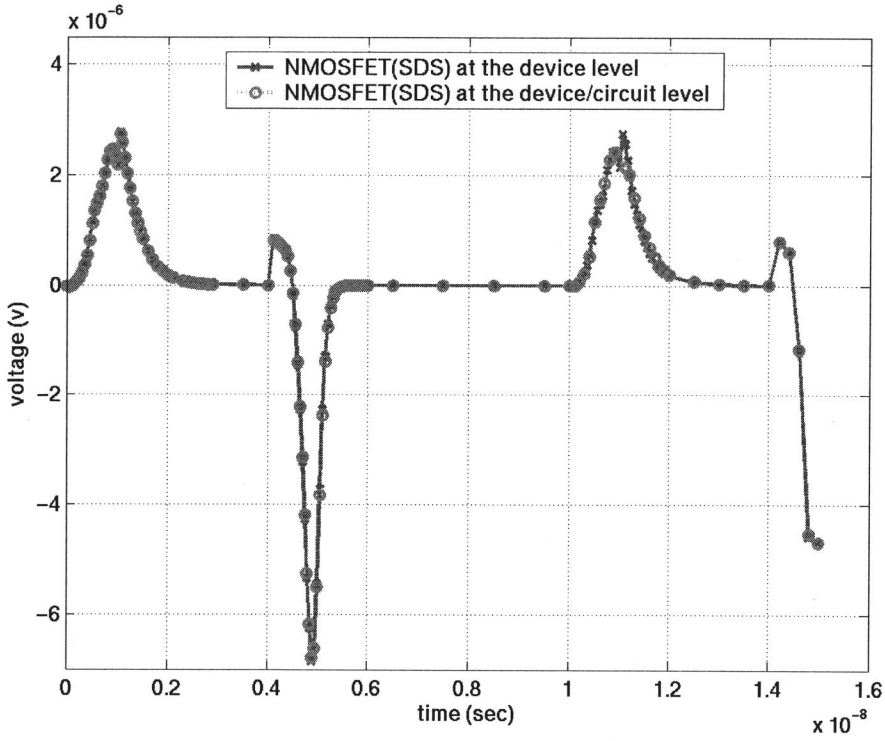

Figure 2-17 Noise waveforms picked up at the P+ substrate tap from the two experiments with SDS NMOS transistors. Simulation results from both experiments agree with each other.

Figure 2-17 shows the noise waveform at the P+ substrate tap at the device level and at the circuit level with the NMOS transistor as a SDS structure. The pull-up injection peak current magnitude is 2.9μA and the pull-down injection peak current magnitude is 6.9μA. Both simulations are in close agreement.

Two conclusions are made from these simulation results. First, the inverter with the DSD NMOS transistor layout injects twice as much noise into the substrate compared to the SDS case. Second, the substrate network connections proposed for both the DSD and SDS NMOS transistor layouts are accurate since the simulation results are in good agreement.

2.3 Summary

In this chapter, substrate noise coupling due to switching of NMOS transistors is analyzed by studying an inverter at the device level. The noise injection from the NMOS transistor is from the drain region. Two layout variants, DSD and SDS, of the NMOS transistor are studied. The noise injection of the inverter with DSD NMOS transistor layout is approximately twice the noise injection with SDS layout. To reduce switching noise, the area of the NMOS drain region should be minimized. Also, substrate current flow lines in the NMOS transistor were used to identify the resistive substrate network and its connections.

3 COUPLING BETWEEN N+-P+ CONTACTS

Existing substrate coupling models are based on coupling between P+ substrate taps. These models are adequate when package inductances are large. However, as the package inductance reduces to values below 0.1nH [1][2], transistor switching noise becomes the dominant source of noise. For a switching NMOS transistor in a digital inverter, the substrate noise is injected from the N+ drain diffusion region. For this reason it is important to examine the coupling from N+ contacts. In this chapter, the difference between the coupling between N-P and P-P contacts is discussed.

3.1 Qualitative Analysis

In Section 3.1.1, the coupling between N-P and P-P contacts is compared qualitatively. The comparison starts from their equivalent circuit schematics. Then, their physical difference is examined in Medici. In Section 3.2.2, the coupling between a single N+ contact and the backplane is compared with that of a P+ contact to demonstrate the self-coupling characteristic of a N+/P+ contacts.

3.1.1 Qualitative Analysis of Coupling Between N+-P+ Contact

Figure 3-1 models the coupling in N-P and P-P structures. Unlike the P-P structure, the N-P structure has a capacitor, $C_{junction}$, between the N+ diffusion region and the p-type substrate.

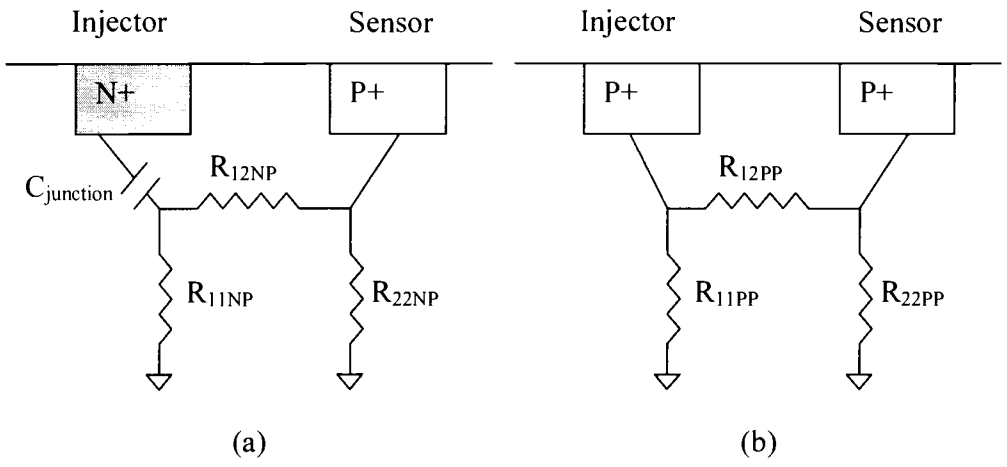

Figure 3-1 Equivalent circuits of (a) coupling between N-P contacts, and (b) coupling between P-P contacts.

Transient simulations of the N-P and P-P structures were performed in Medici to observe the substrate current flow lines. Two comparisons between the N-P and P-P structures are made here. The first structure is made up of a big injector of size 45μm, a small sensor of 1μm, and a spacing of 10μm in each of the N-P and P-P coupling cases. The second structure is made up of a small injector of size 1μm, a small sensor of size 1μm, and a spacing of 10μm in each of the N-P and P-P cases. A sinusoidal input of small amplitude with a small DC offset is applied at the injectors of the N-P and the P-P structures in the simulations. The substrate backplane is kept floating.

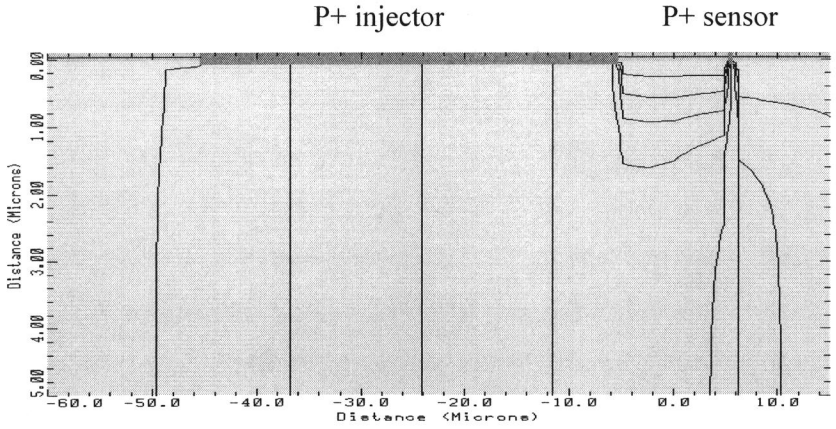

Figure 3-2 Substrate current flow lines in the P-P structure with a P+ injector of size 45μm, a P+ sensor of size 1μm, and a spacing of 10μm. Carriers seek the least impedance path from the injector to the sensor. This figure is zoomed to show details near the substrate surface.

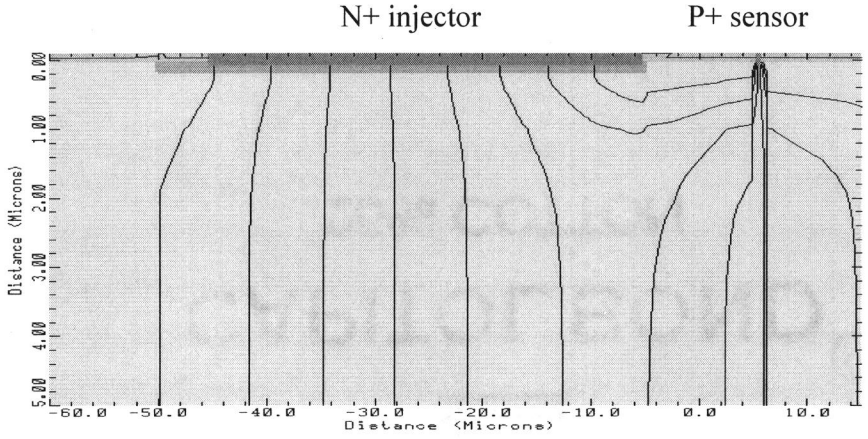

Figure 3-3 Substrate current flow lines in the N-P structure with a N+ injector of size 45μm, a P+ sensor of size 1μm, and a spacing of 10μm. Carriers in the p-type substrate propagate through a longer path to the sensor than those in the P-P structure. This figure is zoomed to show details near the substrate surface.

In Figure 3-2, the P+ injector of size 45μm is a p-type material in the p-type substrate, and hence the majority carriers seek the least impedance path from the injector to the sensor. However, the substrate current flow lines exhibit different traces in Figure 3-3. Since the N+ diffusion region is an n-type material in a p-type substrate, a capacitor exists across the reverse biased pn junction. The electron current dominates on the n-side and the hole current dominates on the p-side. Across the junction capacitor, the displacement of charge varies with the voltage resulting in a displacement current. As a result, the holes on the p-side propagate through a longer path to the sensor as in Figure 3-3. Hence, the cross-coupling resistance is larger in the N-P structure compared to the P-P structure.

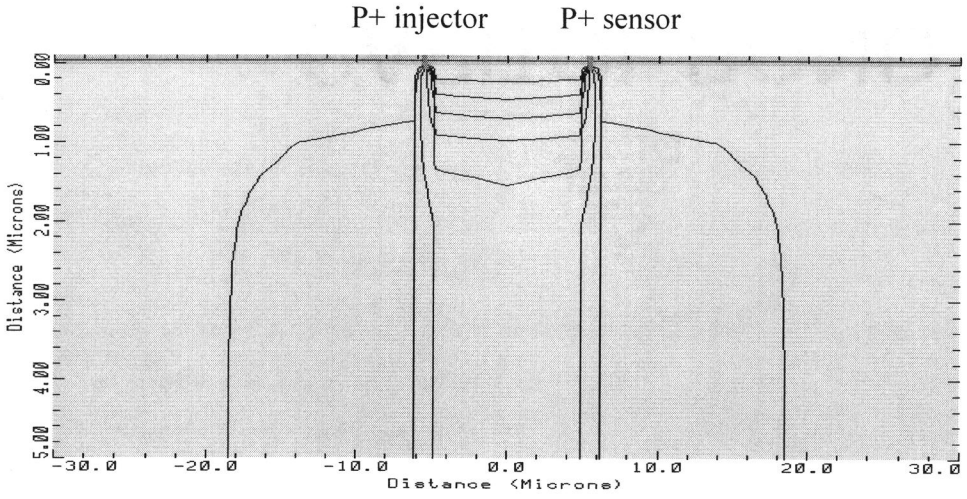

Figure 3-4 Substrate current flow lines in the P-P structure with a P+ injector of size 1μm, a P+ sensor of size 1μm, and a spacing of 10μm. This figure is zoomed to show details.

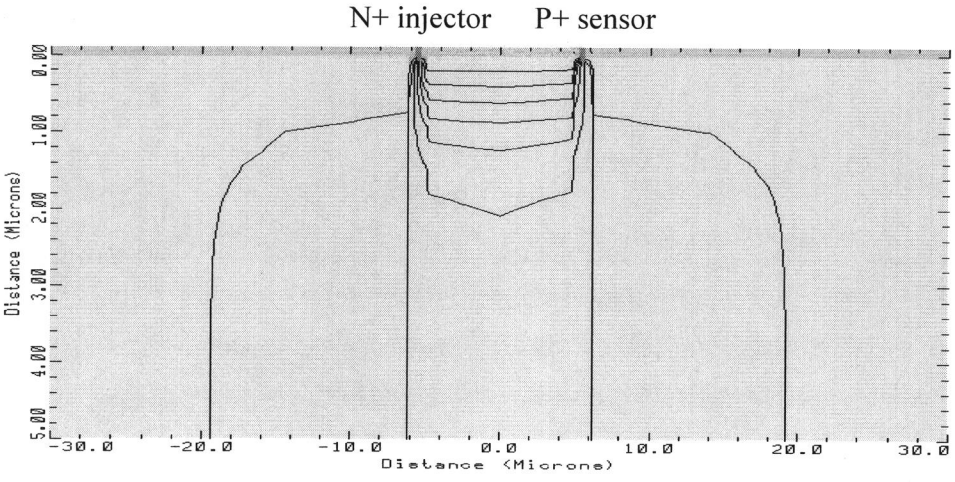

Figure 3-5 Substrate current flow lines in the N-P structure with a N+ injector of size 1μm, a P+ sensor of size 1μm and a spacing of 10μm. This figure is zoomed to show details.

In Figure 3-4, the majority carriers from the P+ injector also flow through the least impedance path to the sensor. Figure 3-5 shows the substrate current flow lines of a N-P structure with a N+ contact of size 1μm, a P+ sensor of size 1μm and a spacing of 10μm. Because the N+ contact is small, the extra distance the holes travel is relatively short compared with the separation. Therefore, from comparison of the traces for the substrate current flow lines in Figure 3-4 and Figure 3-5, carriers in the N-P and P-P structures both travel through similar distances to the sensor. As a result, the resistive network extracted from a N-P structure of a small N+ contact is similar to the resistance values of an equivalent P-P structure regardless of the separation.

3.1.2 Qualitative Analysis of Coupling Between a N+ Contact and the Backplane

Transient analyses similar to those performed in Section 3.1.1 were used to examine the coupling between a N+ contact and the backplane. In these simulations, the substrate is grounded and the contact is of size 25μm and 1μm, respectively. The substrate current flow lines for the N+ contact of size 1μm in Figure 3-6(a) are compared with those of a P+ contact of the same size in Figure 3-6(b). It can be seen that the traces of the current flow lines in these two figures are similar. The substrate current flow lines in Figure 3-6(c) and 3-6(d) are similar for a larger N+/P+ contacts of size 25μm. The self-coupling parameter is the resistance from the bottom of the contact to the backplane and is associated with the contact size. Hence, the self-coupling parameter value of a N+ contact (without the junction capacitance) agrees with that of a P+ contact.

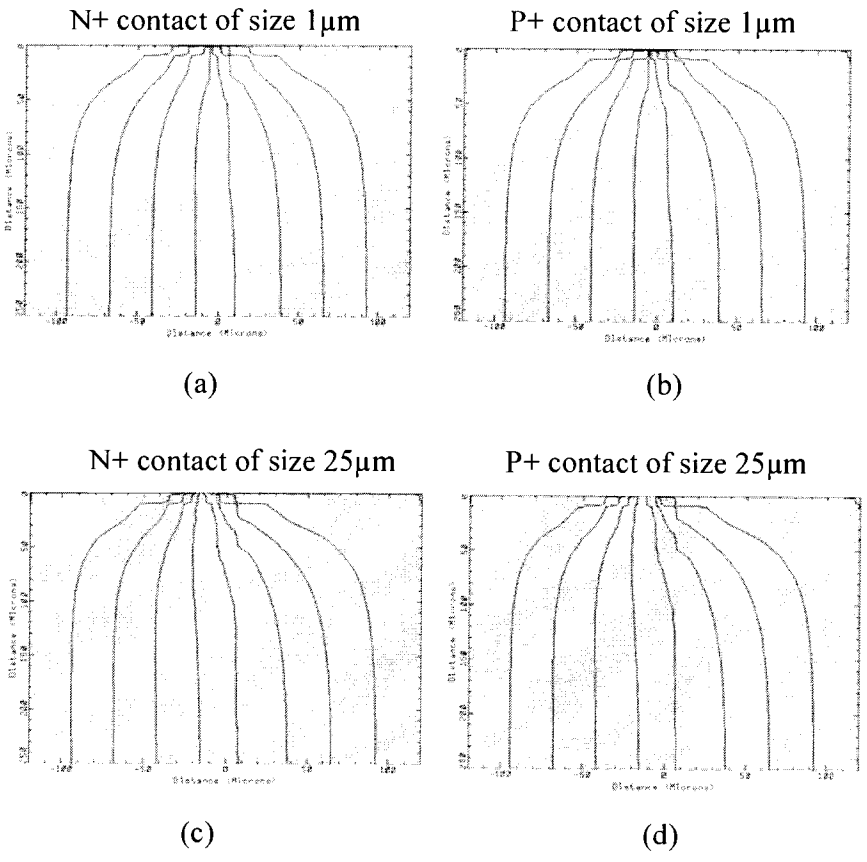

Figure 3-6 (a) Substrate current flow lines of a N+ contact of size 1μm. (b) Substrate current flow lines of a P+ contact of size 1μm. (c) Substrate current flow lines of a N+ contact of size 25μm. (d) Substrate current flow lines of a P+ contact of size 25μm. The backplane is grounded.

3.2 Substrate Resistance Computation for the Coupling Between N-P Contacts

The P-P model based on z-parameters allows for a straight forward method to compute the resistive network for multiple substrate contacts. A similar approach is needed for extracting the resistive network for coupling between N+-P+ contacts. In this section, an extension of the method proposed in [14] for N-P coupling is discussed. The method for extracting the P-P model is summarized in the following three steps.

(1) For N contacts, the z-parameters in the NxN Z matrix (Equation (3.1)) are stamped by considering two contacts at a time.

(2) The Y matrix is computed by inverting the Z matrix as shown in Equation (3.2).

(3) Resistances between the contacts and from a contact to the backplane are computed from the y-parameters as shown in Equation (3.3).

$$Z_{N\times N} = \begin{bmatrix} z_{11} & .. & .. & z_{1(N-1)} & .. \\ : & .. & .. & : & .. \\ : & .. & .. & : & .. \\ z_{(N-1)1} & .. & .. & z_{(N-1)(N-1)} & .. \\ : & .. & .. & : & .. \end{bmatrix} \tag{3.1}$$

$$Y_{N\times N} = Z_{N\times N}^{-1} = \begin{bmatrix} y_{11} & y_{12} & .. & y_{1(N-1)} & y_{1N} \\ : & .. & .. & : & .. \\ : & .. & .. & : & .. \\ y_{(N-1)1} & y_{(N-1)2} & .. & y_{(N-1)(N-1)} & y_{(N-1)N} \\ : & .. & .. & : & .. \end{bmatrix} \tag{3.2}$$

$$R_{N\times N}=\begin{bmatrix} \dfrac{1}{\sum_{j=1}^{N} y_{1j}} & -\dfrac{1}{y_{12}} & .. & -\dfrac{1}{y_{1(N-1)}} & -\dfrac{1}{y_{1N}} \\ : & .. & .. & : & .. \\ : & .. & .. & : & .. \\ -\dfrac{1}{y_{(N-1)1}} & -\dfrac{1}{y_{(N-1)2}} & .. & \dfrac{1}{\sum_{j=1}^{N} y_{(N-1)j}} & -\dfrac{1}{y_{(N-1)N}} \\ : & .. & .. & : & \dfrac{1}{\sum_{j=1}^{N} y_{Nj}} \end{bmatrix} \tag{3.3}$$

For the N-P coupling structure, a junction capacitor has to be included. The computation of the resistances does not seem obvious at a first glance. However, after a slight modification on the Z matrix of the N-P coupling structure, Equations (3.1)-(3.3) can also be applied to compute the resistance values. Figure 3-7(a) shows the equivalent circuit of a N-P structure. Its Z matrix is constructed in Equation (3.4). By comparing the 2x2 Z matrices of N-P and P-P structures, the only difference is the z_{11} parameter of Z_{2x2NP}, which has an imaginary part from the junction capacitor. After removing this imaginary part in the z_{11} parameter, the resistance values of the N-P structure can be easily computed in the same manner as those for the P-P structure. The junction capacitance in the N-P coupling structure can be computed from the imaginary part in the z_{11} parameter of Z_{2x2NP}.

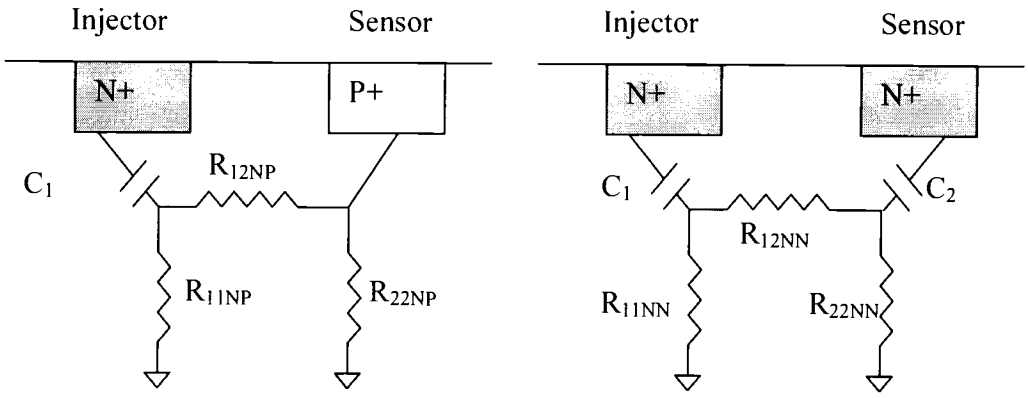

Figure 3-7 (a) N-P coupling equivalent circuit, and (b) N-N coupling equivalent circuit.

$$Z_{2\times 2\,NP} = \begin{bmatrix} \dfrac{(R_{12\,NP}+R_{22\,NP})R_{11\,NP}}{R_{11\,NP}+R_{12\,NP}+R_{22\,NP}} - \dfrac{j}{\omega C_1} & \dfrac{R_{11\,NP}R_{22\,NP}}{R_{11\,NP}+R_{12\,NP}+R_{22\,NP}} \\ \dfrac{R_{11\,NP}R_{22\,NP}}{R_{11\,NP}+R_{12\,NP}+R_{22\,NP}} & \dfrac{(R_{11\,NP}+R_{12\,NP})R_{22\,NP}}{R_{11\,NP}+R_{12\,NP}+R_{22\,NP}} \end{bmatrix} \tag{3.4}$$

$$Z_{2\times 2\,PP} = \begin{bmatrix} \dfrac{(R_{12\,PP}+R_{22\,PP})R_{11\,PP}}{R_{11\,PP}+R_{12\,PP}+R_{22\,PP}} & \dfrac{R_{11\,PP}R_{22\,PP}}{R_{11\,PP}+R_{12\,PP}+R_{22\,PP}} \\ \dfrac{R_{11\,PP}R_{22\,PP}}{R_{11\,PP}+R_{12\,PP}+R_{22\,PP}} & \dfrac{(R_{11\,PP}+R_{12\,PP})R_{22\,PP}}{R_{11\,PP}+R_{12\,PP}+R_{22\,PP}} \end{bmatrix} \tag{3.5}$$

$$Z_{2\times 2\,NN} = \begin{bmatrix} \dfrac{(R_{12\,NN}+R_{22\,NN})R_{11\,NN}}{R_{11\,NN}+R_{12\,NN}+R_{22\,NN}} - \dfrac{j}{\omega C_1} & \dfrac{R_{11\,NN}R_{22\,NN}}{R_{11\,NN}+R_{12\,NN}+R_{22\,NN}} \\ \dfrac{R_{11\,NN}R_{22\,NN}}{R_{11\,NN}+R_{12\,NN}+R_{22\,NN}} & \dfrac{(R_{11\,NN}+R_{12\,NN})R_{22\,NN}}{R_{11\,NN}+R_{12\,NN}+R_{22\,NN}} - \dfrac{j}{\omega C_2} \end{bmatrix} \tag{3.6}$$

Figure 3-7(b) shows the equivalent circuit for a N-N coupling structure. Its Z matrix is shown in Equation (3.6). After removing the imaginary parts of z_{11} and z_{22} parameters, the resistances of this N-N structure can easily be computed as well. The junction capacitances, C_1 and C_2, can also be extracted from the imaginary parts of z_{11} and z_{22} parameters, respectively.

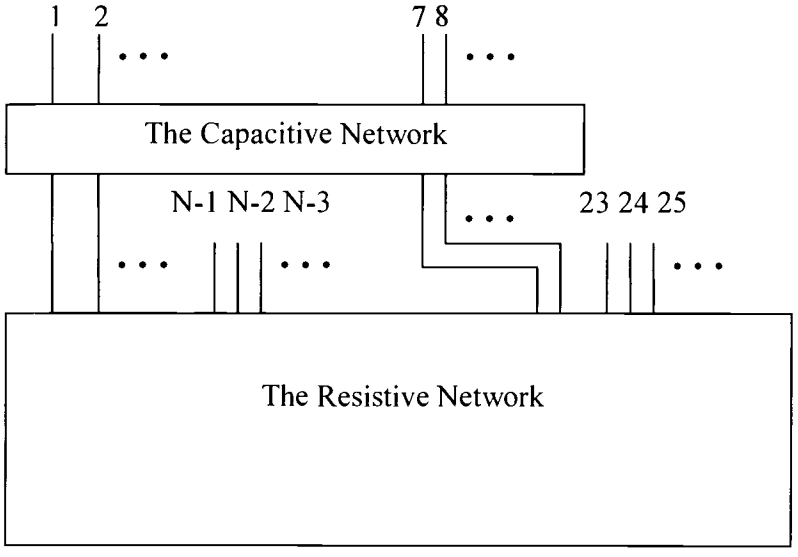

Figure 3-8 The substrate network of multiple N+ and P+ contacts decomposed into the summation of a resistive network and a capacitive network

For a circuit with multiple N+ and P+ contacts, the equivalent network can be decomposed into a capacitive network and a resistive network shown in Figure 3-8. After the capacitive network, or equivalently, the imaginary portions of the z_{ii} parameters are removed, the resistance values of the network can be computed by applying Equations (3.1)-(3.3).

The three steps to compute the resistance values from a network containing N+ contacts are summarized as follows.

(1) Construct the Z matrix by considering 2 contacts at a time and then remove the imaginary portions of the z-parameters.

(2) Invert Z to obtain the Y matrix.

(3) Compute the resistance values from the y-parameters as in Equation (3.3).

In this section, the resistance computation method for the N-P coupling leads to the observation that the real part of the z-parameter is sufficient for studying the N-P coupling structure.

3.3 Quantitative Analysis

In this section, quantitative analyses of coupling between N+-P+ and P+-P+ contacts are discussed. The resistance values of the N-P coupling are computed based on the computation method proposed in Section 3.2. Section 3.3.1 examines coupling between N+-P+ contacts at frequencies of 10MHz, 1GHz, and 2GHz. From these simulation results, self-coupling parameters and cross-coupling parameters are extracted from N-P and P-P structures at 100MHz in Section 3.3.2 and Section 3.3.3, respectively.

3.3.1 Coupling Between N+-P+ Contacts at Different Frequencies

In Figure 3-9 and Figure 3-10, z_{11NP} and R_{11NP} values are obtained from symmetric N+-P+ contacts of sizes 45μm and 1μm at 10MHz, 1GHz, and 2GHz, respectively. The z_{11NP} parameter is the open-circuit parameter of the N+ contact in the N-P equivalent circuit. R_{11NP} is the resistance from the N+ contact to the backplane in the N-P structure. In these two figures, it can be seen that the z_{11NP} (R_{11NP}) values do not change from a low frequency of 10MHz to a high frequency of 2GHz.

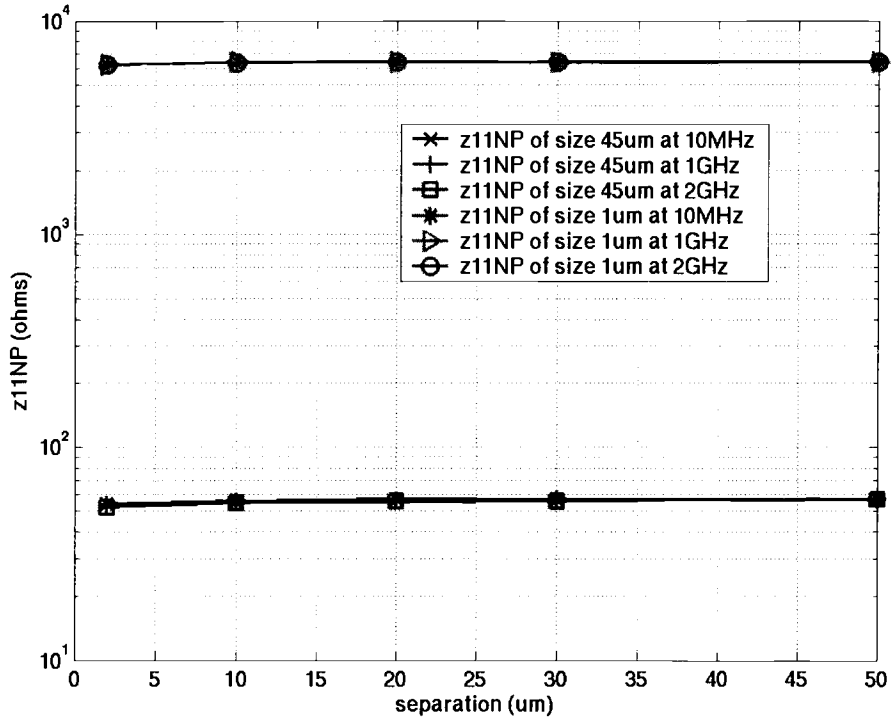

Figure 3-9 z_{11NP} extracted from symmetric N+-P+ contacts of sizes 45μm and 1μm at 10MHz, 1GHz, and 2GHz, respectively.

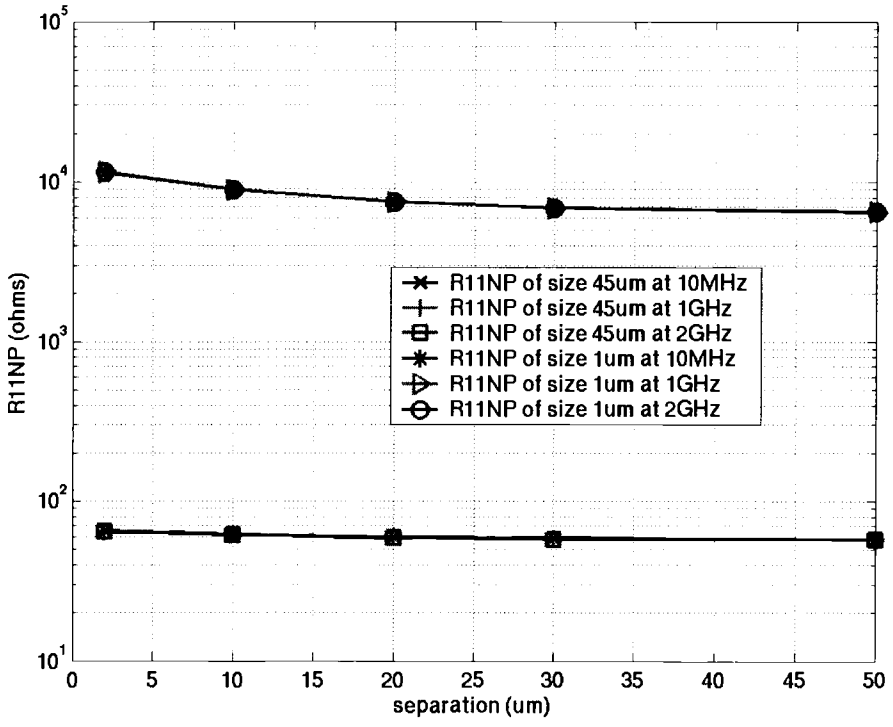

Figure 3-10 R_{11NP} extracted from symmetric N+-P+ contacts of sizes 45μm and 1μm at 10MHz, 1GHz, and 2GHz, respectively.

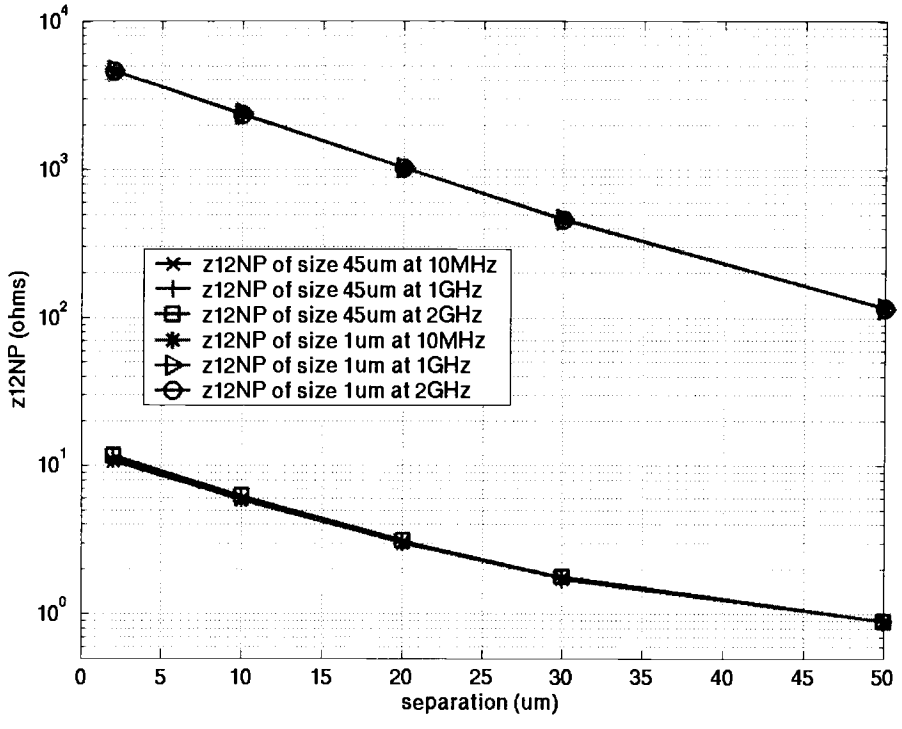

Figure 3-11 z_{12NP} extracted from symmetric N+-P+ contacts of sizes 45μm and 1μm at 10MHz, 1GHz, and 2GHz, respectively.

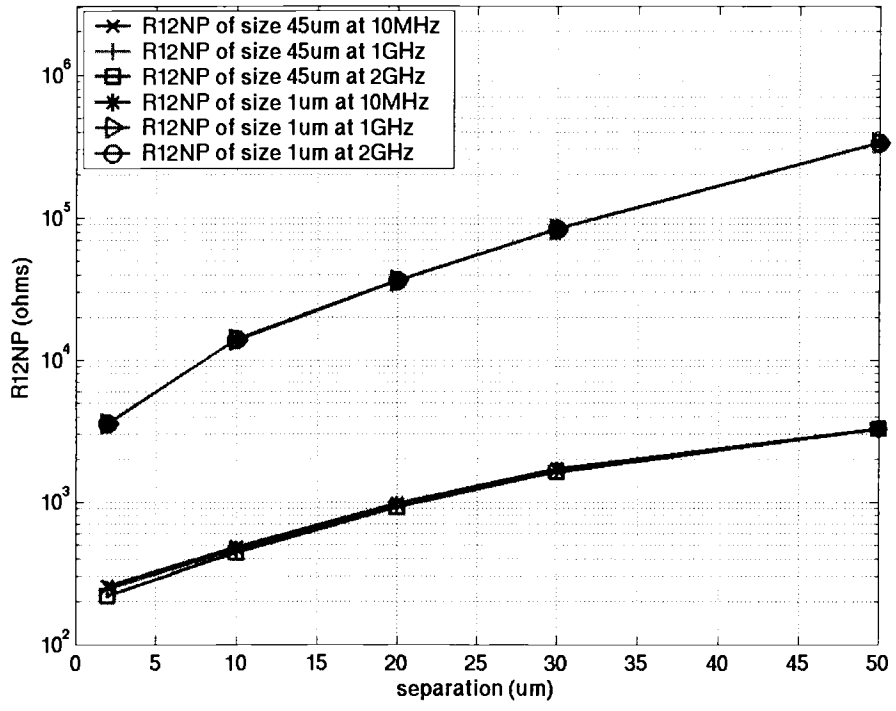

Figure 3-12 R_{12NP} extracted from symmetric N+-P+ contacts of sizes 45μm and 1μm at 10MHz, 1GHz, and 2GHz, respectively.

Figure 3-11 and Figure 3-12 show z_{12NP} and R_{12NP} values extracted from symmetric N+-P+ contacts of sizes 45μm and 1μm at 10MHz, 1GHz, and 2GHz, respectively. In these two figures, it can also be seen that from a frequency of 10MHz to a frequency of 2GHz, there is a negligible difference in z_{12NP} (R_{12NP}) values.

The focus of the N-P coupling in this thesis is aimed at low frequencies where the substrate can be assumed as a resistive network [3][20]. Figure 3-9 to Figure 3-12 all show that the coupling parameters at different frequencies are in close agreement. Hence, in Section 3.3.2 and Section 3.3.3, N-P and P-P structures

are simulated at 100MHz to compare their self-coupling and cross-coupling parameters.

3.3.2 Self-Coupling Parameters of the N-P and P-P Structures

Self-coupling parameters in this section are extracted from N-P and P-P structures at 100MHz. In Section 3.2, it was shown that the real portion of the z_{11NP} value has sufficient information for extracting the resistance of the N-P network. Hence, only the real portion of the complex z_{11NP} is considered and will be simply called z_{11NP}. The z_{11PP} parameter is the open-circuit parameter of the P+ contact in the P-P equivalent circuit. R_{11PP} is the resistance from the P+ contact to the backplane in the P-P structure. Small symmetric contacts of size 1μm and large symmetric contacts of size 45μm are compared in this section. Figure 3-13 shows z_{11NP} and z_{11PP} values of symmetric contacts of sizes 1μm and 45μm as a function of separation. For the same size of contact, the z_{11NP} value agrees with the z_{11PP} value regardless of the separation. The self-coupling parameter of symmetric contacts of size 45μm shows a smaller value. This is because a larger contact has a smaller resistance to the backplane. Figure 3-14 shows the percentage errors computed by comparing the z_{11NP} and z_{11PP} values of contact sizes 1μm and 45μm, respectively.

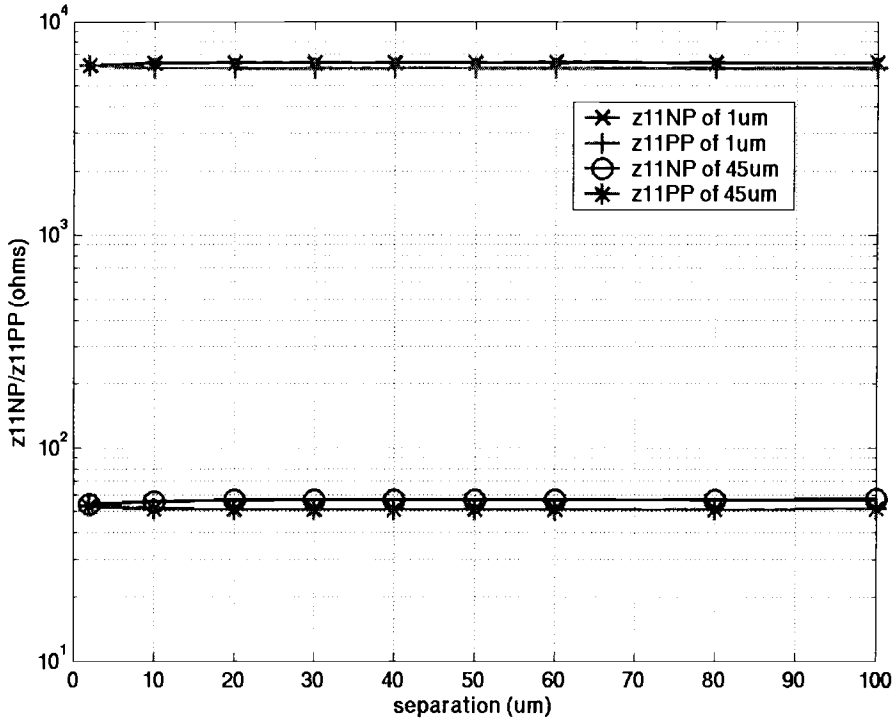

Figure 3-13 z_{11NP} and z_{11PP} for symmetric contacts of sizes 1μm and 45μm as a function of separation at 100MHz.

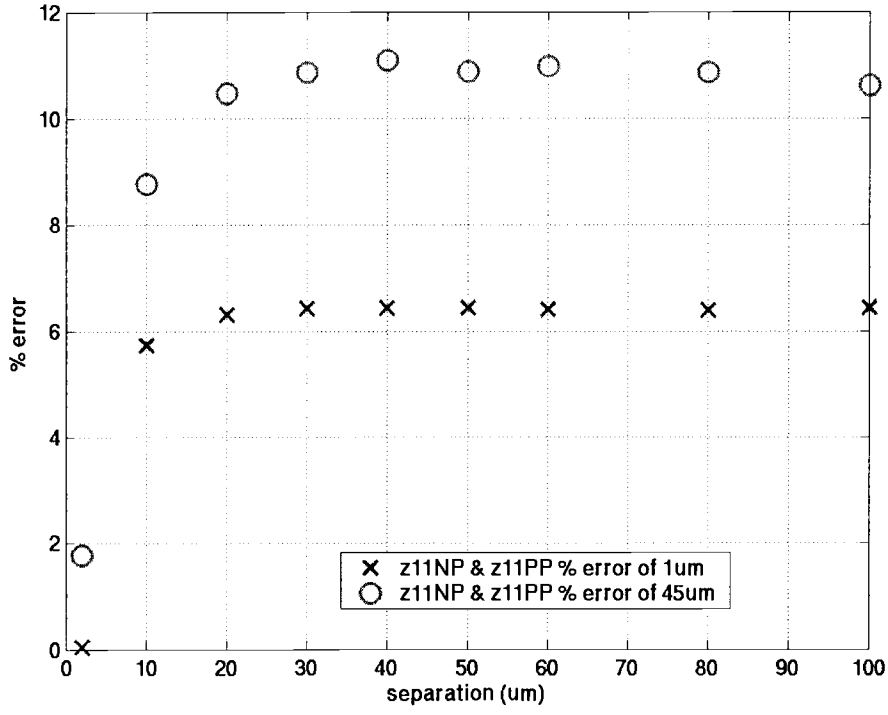

Figure 3-14 Percentage errors computed by comparing the z_{11NP} and z_{11PP} values of the same contact size in Figure 3-11 simulated at 100MHz.

In Figure 3-14, the computed errors are below 12%. Figure 3-15 shows R_{11NP} and R_{11PP} values of symmetric contacts of sizes 1μm and 45μm as a function of separation. From this graph, R_{11NP} and R_{11PP} values agree with each other. The percentage errors of R_{11NP} and R_{11PP} are computed and plotted in Figure 3-16. The overall errors in this figure are less than 15%.

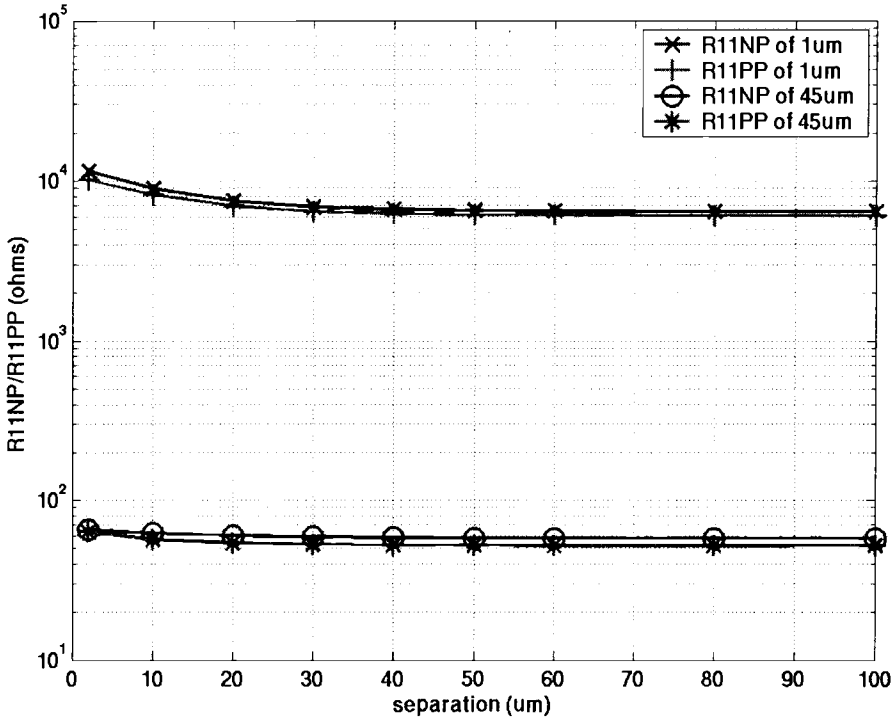

Figure 3-15 R_{11NP} and R_{11PP} for symmetric contacts of sizes 1μm and 45μm at 100MHz.

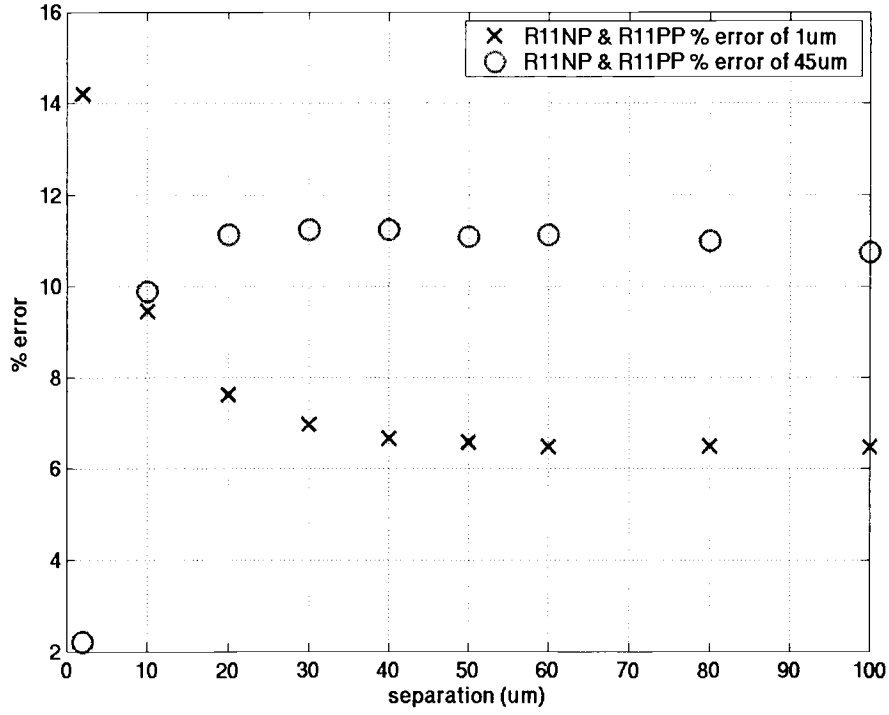

Figure 3-16 Percentage errors computed by comparing the R_{11NP} and R_{11PP} values of the same contact size in Figure 3-13 at 100MHz.

In summary, the self-coupling parameters, z_{11NP} and z_{11PP} are in good agreement. So are the self-coupling parameters, R_{11NP} and R_{11PP}. These results are expected from the qualitative analysis in Section 3.1.2.

3.3.3 Cross-Coupling Parameters of N-P and P-P Structures

In this section, the cross-coupling parameters, z_{12NP}, z_{12PP}, R_{12NP} and R_{12PP}, are extracted from N-P and P-P structures at 100MHz. Figure 3-17 shows the cross-coupling z-parameter values of symmetric contacts of size 1μm. The cross-coupling z-parameter values of symmetric contacts of size 45μm are plotted in Figure 3-18.

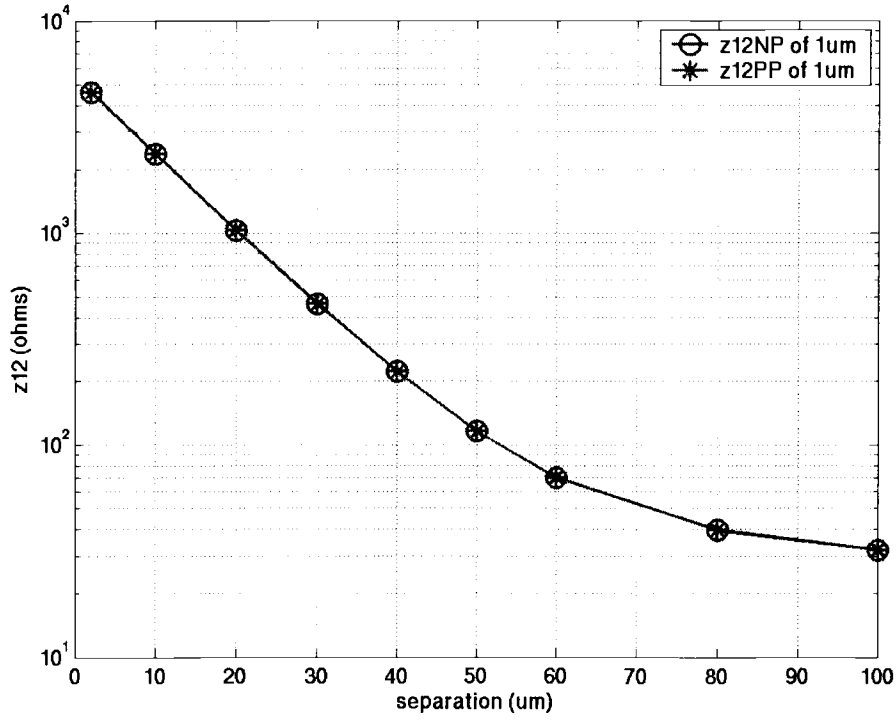

Figure 3-17 z_{12NP} and z_{12PP} for symmetric contacts of size 1μm as a function of separation at 100MHz.

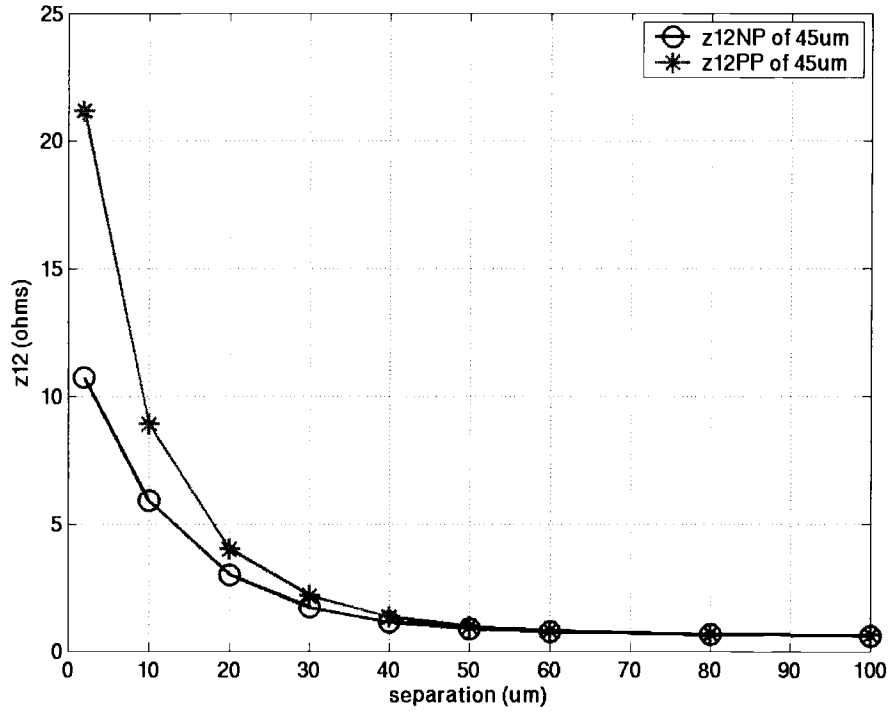

Figure 3-18 z_{12NP} and z_{12PP} for symmetric contacts of size 45μm as a function of separation at 100MHz.

In Figure 3-17, the cross-coupling z-parameter values for small symmetric contacts show little difference between the N-P and P-P structures. However from Figure 3-18, it can be seen that the cross-coupling z-parameter values for larger symmetric contacts show significant difference between the two cases for short separations less than 10μm. As the separation increases, the difference reduces. Figure 3-19 shows the percentage errors computed by comparing the cross-coupling z-parameter values of symmetric contacts of sizes 1μm and 45μm, respectively.

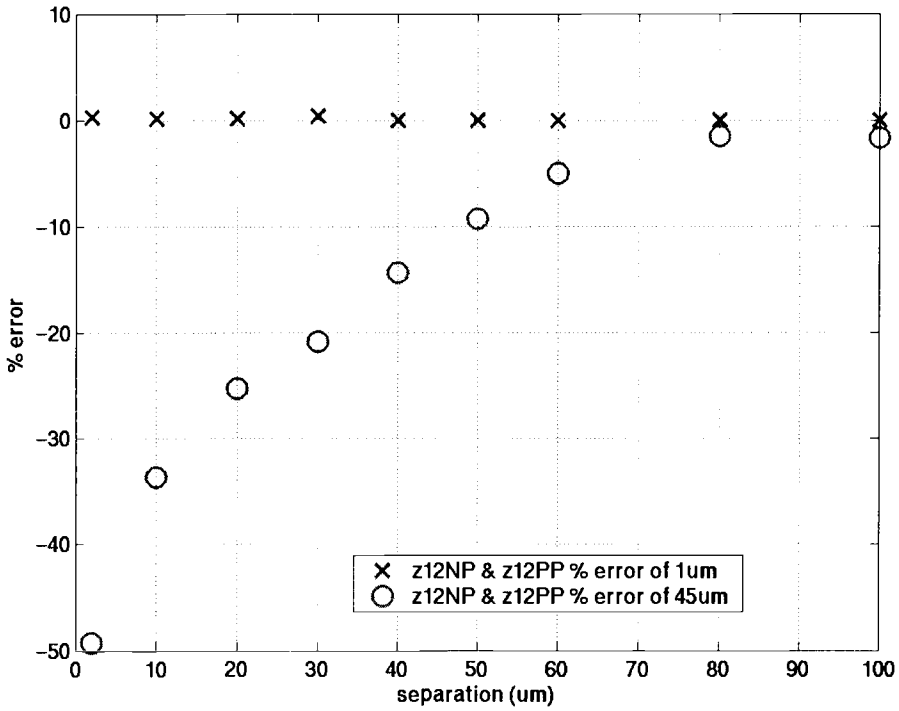

Figure 3-19 Percentage errors of z_{12NP} and z_{12PP} values of symmetric contacts of sizes 1μm and 45μm at 100MHz.

In Figure 3-19, it is seen that for small symmetric contacts the percentage errors between z_{12NP} and z_{12PP} values are close to 0%. For large symmetric contacts, the percentage error in the worst case is 50% at a short separation of 2μm. The percentage error decreases as the separation increases.

Figure 3-20 shows R_{12NP} and R_{12PP} values of symmetric contacts of sizes 1μm and 45μm. For the same size of the symmetric contacts with the same separation, the R_{12NP} value is larger than the R_{12PP} value. As the separation increases, both R_{12NP} and R_{12PP} values increase. The percentage errors of R_{12NP} and R_{12PP} are computed and plotted in Figure 3-21.

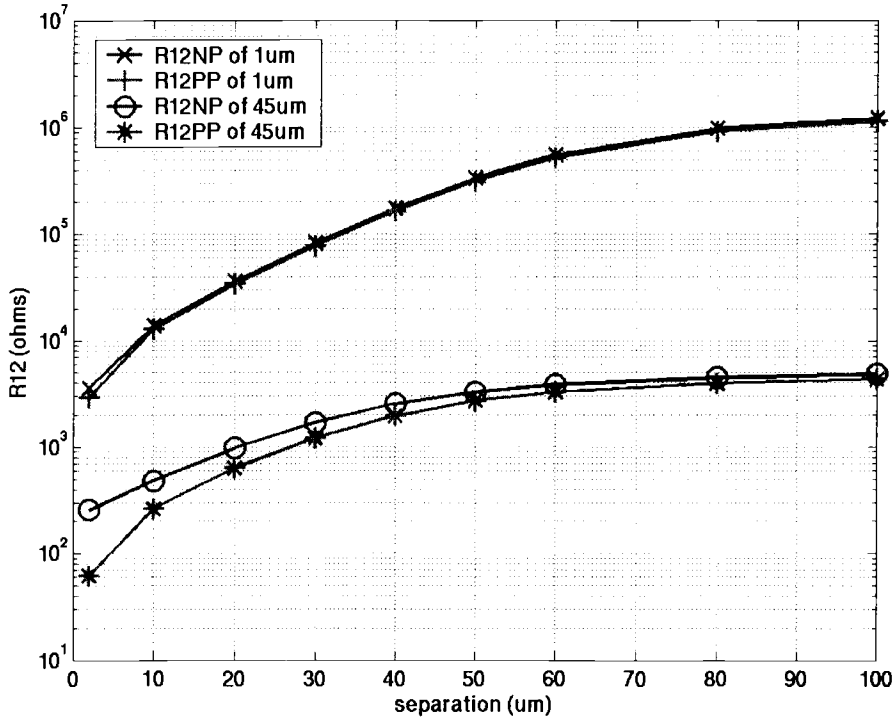

Figure 3-20 R_{12NP} and R_{12PP} for symmetric contacts of sizes 1μm and 45μm at 100MHz.

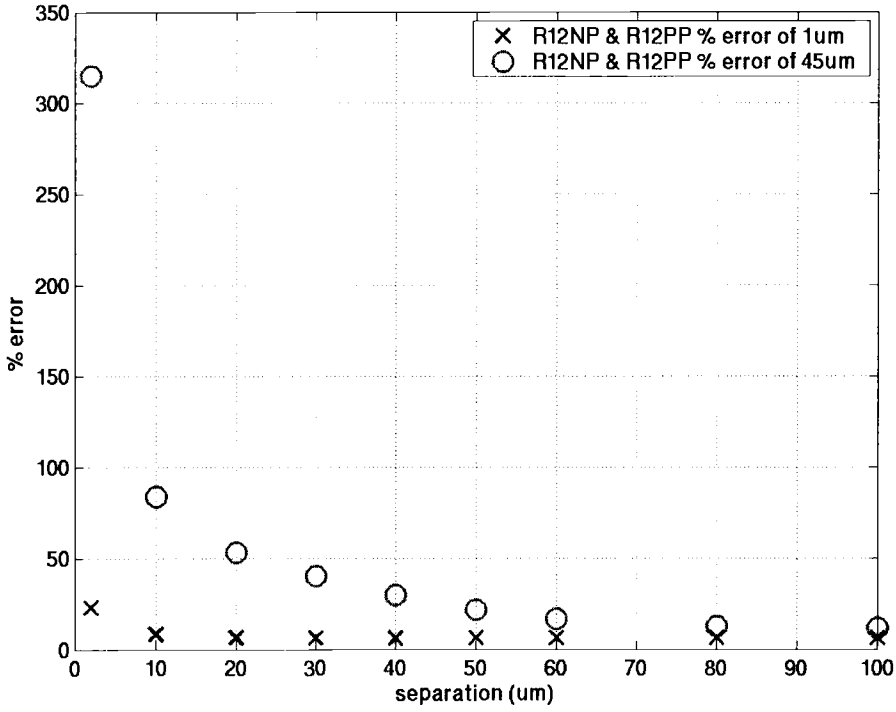

Figure 3-21 Percentage errors of R_{12NP} and R_{12PP} for symmetric contacts of sizes 1μm and 45μm at 100MHz.

Figure 3-21 shows that for small symmetric contacts the difference between the R_{12NP} and R_{12PP} values is below 25%. However, for larger symmetric contacts, the difference between the R_{12NP} and R_{12PP} values is significantly large at a separation of 2μm. As the separation increases, the difference between them reduces.

In summary, the cross-coupling parameters of the N-P structure differ significantly from those of the P-P structure, especially at a short separation. These results are expected and the physical explanations have been provided in Section 3.1.1.

3.4 The Concept of Virtual Separation

Since the self-coupling parameters of the N-P and P-P structures are similar, the focus of the new N-P model is on the modeling of cross-coupling parameters, R_{12NP} or z_{12PP}. Figure 3-18 shows that the z_{12NP} value is much less than the z_{12PP} value for a large N+ contact with small separations. Also, Figure 3-20 shows that for the same size contacts, R_{12NP} value is much larger than R_{12PP} for a large N+ contact with a small separation. Similar to R_{12PP}, R_{12NP} increases as the separation increases and decreases as the contact size increases. All of these suggest that the cross-coupling parameter of the N-P structure can be modeled by the cross-coupling parameter of the P-P structure using the concept of a larger virtual separation.

The virtual separation compensates for the differences between the N-P and P-P couplings. The major benefit of this modeling idea is that only a small number of N-P structures are required for the new model. The rest of the N-P coupling effects are described by the P-P coupling model.

3.5 Summary

In this chapter, the coupling between N+-P+ contacts is examined both qualitatively and quantitatively. A simple method is proposed to extract the resistance values of multiple N+ and P+ contacts. It has been shown that the P-P model can be used to describe the N-P coupling for small N+ contacts. Also, the P-P model can be used to describe the N-P coupling for large N+ contacts at a large separation from the neighboring contacts. Since z_{12NP} and z_{12PP} have a similar dependence on the contact geometry and the spacing, the N-P coupling can be modeled by an existing P-P model with a larger virtual separation. The next chapter develops an equation for the virtual separation.

4 A NEW N-P MODEL DERIVED FROM THE P-P MODEL WITH VIRTUAL SEPARATIONS

In Chapter 3, it was illustrated that z_{11NP} is similar to z_{11PP} which depends on the contact area and perimeter as described in [12]-[14]. The values of the R_{11NP} and R_{11PP} are in agreement as well. Hence, the self-coupling parameter of a N+ contact can be obtained from the P-P model. The z_{12NP} value exhibits differences from the z_{12PP} value depending on the contact size and the spacing from the neighboring contacts. z_{12NP} value is smaller than z_{12PP} value because in the N-P structure the noise propagates through a longer path to the sensor. Therefore, the modeling of the new N-P model focuses on the cross-coupling parameter. Since the characteristics of both the z_{12NP} and z_{12PP} parameters are similar, the z_{12NP} parameter is modeled by an existing P-P model with a larger virtual separation. Section 3.3.1 has showed that the coupling parameters of the same N-P structure are in close agreement at different frequencies (10MHz to 2GHz). In this chapter, z_{12NP} and z_{12PP} are obtained from N-P and P-P structures at 100MHz, respectively. The development of the N-P model for the virtual separation is described.

4.1 Model for the Virtual Separation

The idea of modeling the z_{12NP} parameter by the z_{12PP} parameter with a larger virtual separation is demonstrated in Figure 4-1. The contacts in the P-P and N-P structures are symmetric. To model the z_{12NP} parameter, an N+ contact is considered as a P+ contact. However, the spacing from this virtual P+ contact and the other P+ contact is larger. In this section, the relationship of the virtual separation, the contact geometry, and the actual separation is established. From this relationship, an equation for the virtual separation is developed. Also, the types of the N-P test structures required for extracting the virtual separation are discussed.

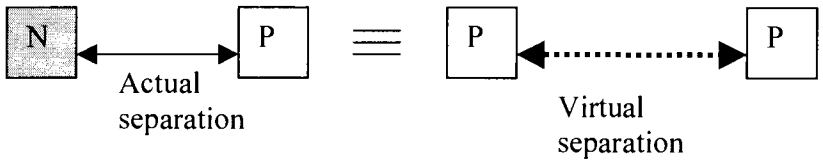

Figure 4-1 Demonstration of the concept of virtual separation. The contacts are symmetric. The N-P coupling is modeled by P-P coupling with a larger virtual separation.

4.1.1 Relationship of the Virtual separation, the Actual Separation and the N+ Contact Size

In Section 3.1.1, it was shown that in the N-P coupling, noise current propagates through a longer path to the sensor. The extra distance the carriers travel is related to the size of the N+ contact. When the separation between the contacts is much larger than the size of the N+ contact, z_{12NP} is similar to z_{12PP} as shown in Section 3.3.3. Hence, based on the analysis in Chapter 3, it can be concluded that the virtual separation depends on both the N+ contact size and the actual separation.

The z_{12NP} and z_{12PP} parameters obtained from symmetric contacts at 100MHz are plotted as a function of the N+ contact size in a N-P structure and the P+ contact size in a P-P structure, respectively in Figure 4-2 and Figure 4-3. Each curve represents z_{12} values for the same separation. Since the simulations are done in 2-D and the contacts are symmetric, the area is computed as the square of the contact width. For a fixed area, the z_{12} value decreases as the separation increases. The trends in these two figures are similar except for the differences in values. The percentage errors of z_{12NP} and z_{12PP} are plotted in Figure 4-4. For structures with small separations, the percentage errors increase as the N+ contact size increases.

However, for coupling structures with large separations, the percentage errors are small regardless of the N+ contact size.

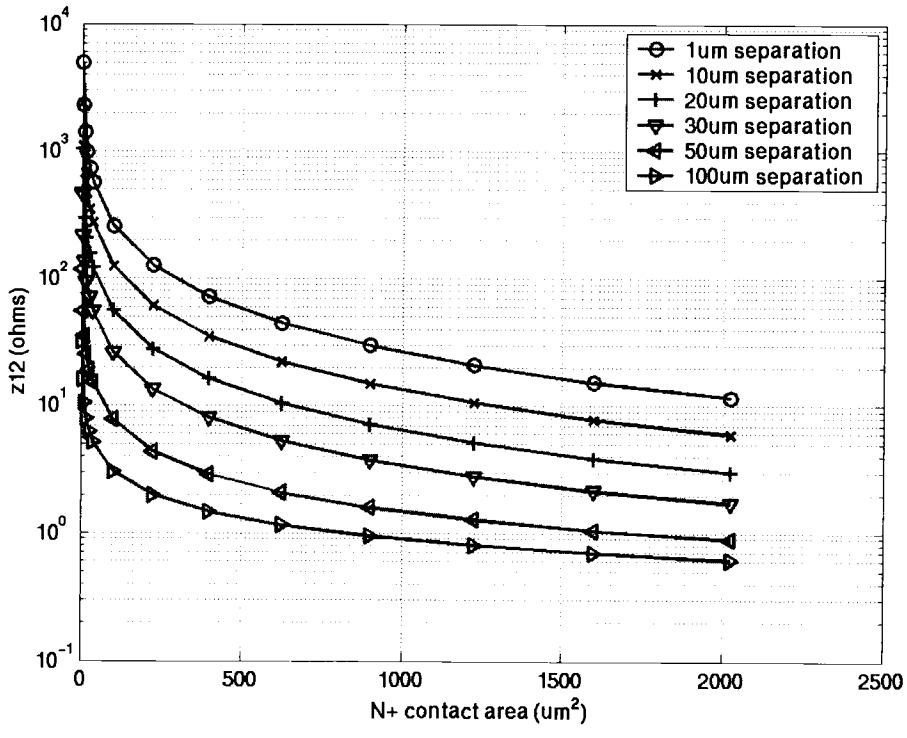

Figure 4-2 z_{12NP} as a function of N+ contact size at 100MHz. For a fixed N+ contact size, the z_{12NP} value decreases as the separation increases.

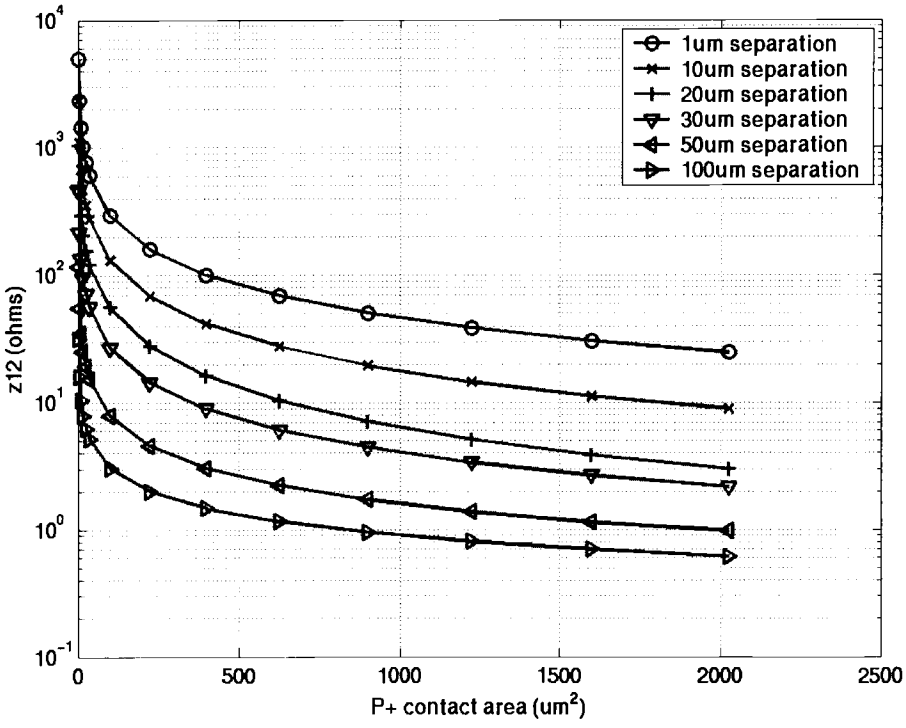

Figure 4-3 z_{12PP} as a function of P+ contact size at 100MHz. For a fixed P+ contact size, the z_{12PP} value decreases as the separation increases.

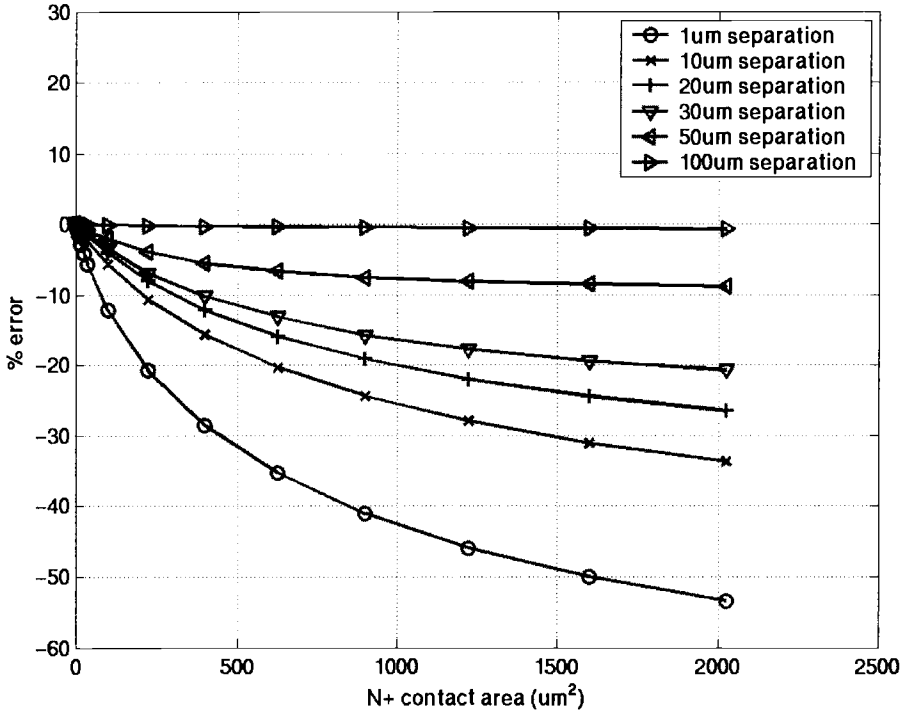

Figure 4-4 Percentage errors of z_{12NP} and z_{12PP} values shown in Figure 4-2 and Figure 4-3. For coupling structures with small separations, the error increases as the N+ contact size increases. However, for coupling structures with large separations, the errors are small regardless of the N+ contact size.

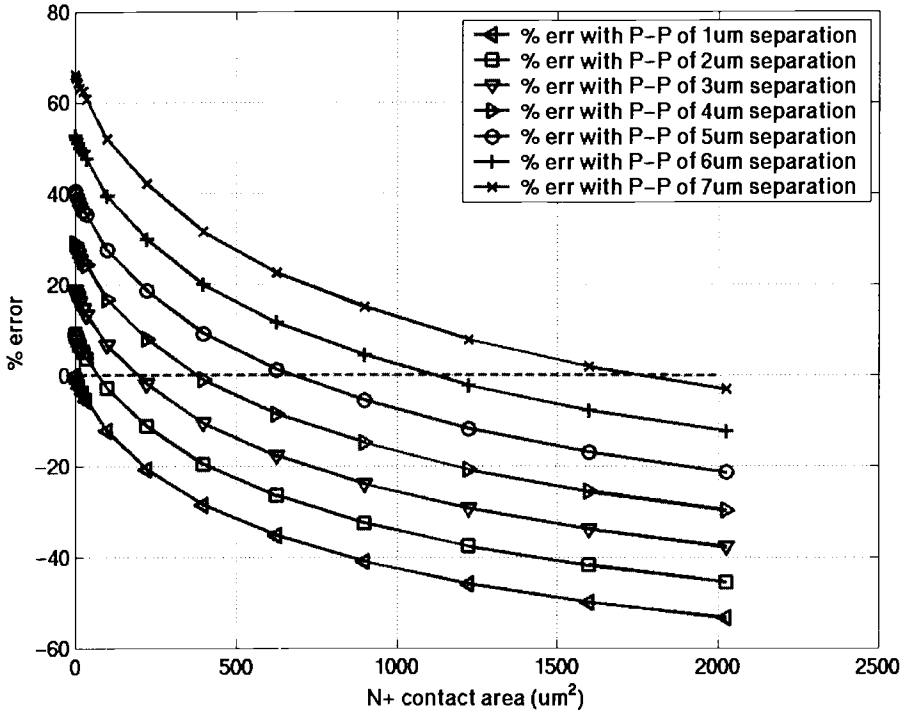

Figure 4-5 Percentage errors for 1μm separation of the N-P structure in Figure 4-2 with curves with larger separations of the P-P structure in Figure 4-3. This shows the virtual separation as a function of N+ contact size for the N-P coupling structure of 1μm separation.

To determine the virtual separation, the percentage error of the z_{12NP} values with a fixed separation and the z_{12PP} values with various separations are computed. Figure 4-5 shows an example of taking z_{12NP} values of 1μm separation in Figure 4-2 and computing the error percentages with z_{12PP} values at various separations. From Figure 4-5, it can be seen that a virtual separation of 7μm is required when the N+ contact size is approximately $1750\mu m^2$. For N-P structures with other separations, the virtual separation is found in a similar manner. Figure 4-6 shows the virtual separation as a function of the N+ contact size. In this figure, it is observed that the curve for an actual separation of 1μm has a larger curvature than

the rest of the curves and as the actual separation increases, the curves become flatter. This is due to the fact that the extra distance the carriers travel increases with the N+ contact size. Hence, for a small actual separation, a larger virtual separation is required to compensate for the large difference in the z_{12NP} and z_{12PP} values.

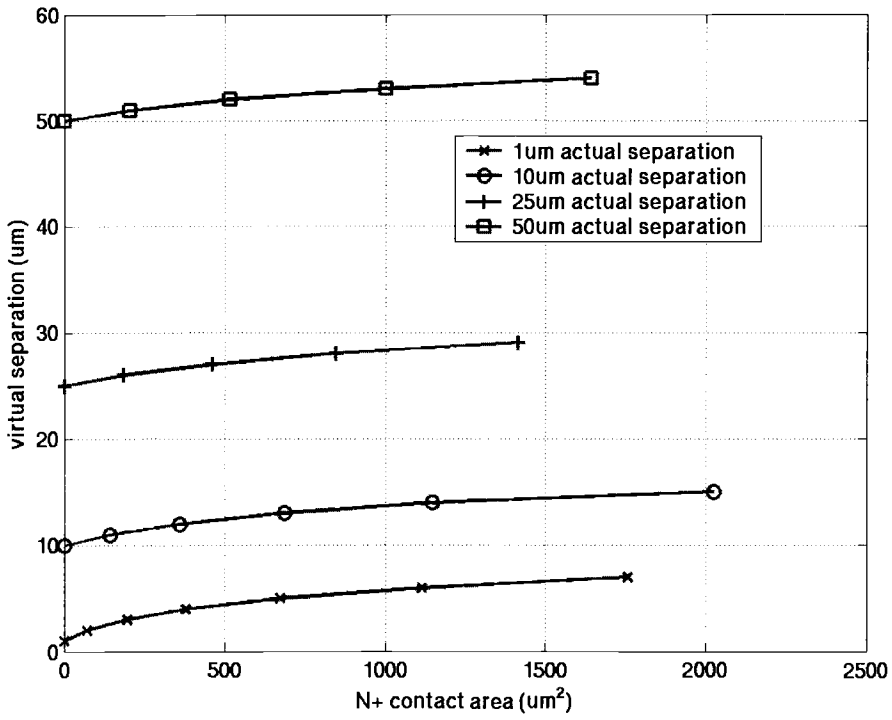

Figure 4-6 Virtual separation as a function of the N+ contact size.

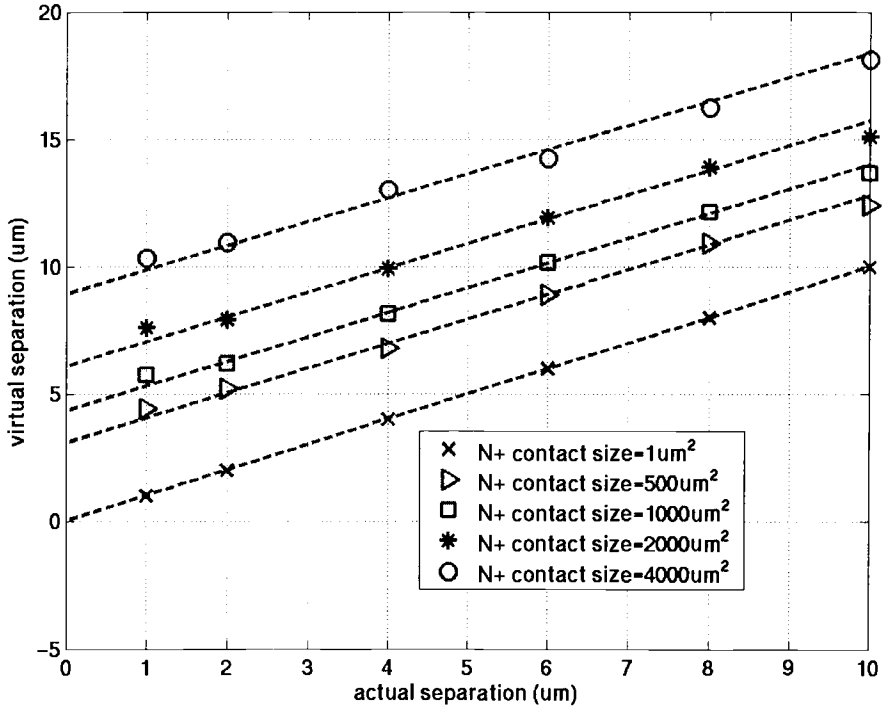

Figure 4-7 Virtual separation as a function of the actual separation below 10μm. The graph shows a nearly linear relationship between the virtual separation and the actual separation. The intercepts and the slopes of the curves are dependent on the N+ contact size.

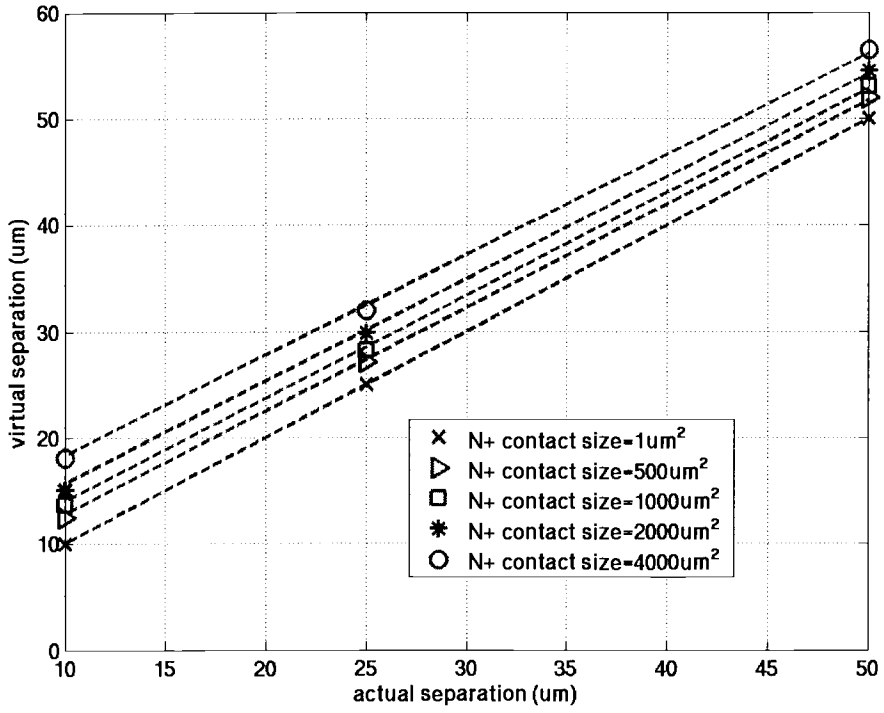

Figure 4-8 Virtual separation as a function of the actual separation from 10μm to 50μm. The graph shows a nearly linear relationship between the virtual separation and the actual separation.

Figure 4-7 and Figure 4-8 show that the virtual separation and the actual separation have a nearly linear relationship. The y-intercept and the slope of the curve are dependent on the N+ contact size.

As the N+ contact size increases, the y-intercept of the curve increases. When the N+ contact size is extremely small, the effect caused by carriers traveling a longer distance is insignificant so that the P-P model can be used to model the N-P coupling. Hence, the curve of N+ contact size of $1\mu m^2$ shows a y-intercept of 0. For a large N+ contact, the effect caused by carriers traveling a longer distance is

significant at a short separation from the neighboring contact. As a result, a larger virtual separation is needed to compensate for the difference. Hence, the y-intercept increases with the size of the N+ contact.

As the N+ contact size increases, the slope of the curve slightly decreases in both Figure 4-7 and Figure 4-8. For a large N+ contact with a much larger separation from the neighboring contact, the extra distance carriers travel is much less than the separation. In this case, the cross-coupling parameter is dependent on the separation mostly. Hence, the virtual separation approximates to the actual separation for a large actual separation. Hence, the slope of the curve decreases as the N+ contact size increases.

4.1.2 An Equation for the Virtual Separation

In Section 4.1.1, it was shown that the virtual separation and the actual separation have a linear relationship. This relationship is given in Equation (4.1). The y-intercept, β, and the slope, α, are dependent on the N+ contact size.

$$Virtual\_Separation = \alpha \times Actual\_Separation + \beta \tag{4.1}$$

In Figure 4-9, α is plotted as a function of the N+ contact size. When the N+ contact area is extremely small, α is equal to 1 due to the small extra distance traveled by the carriers. As the N+ contact area increases, α decreases. Equation (4.2) describes the relationship of the N+ contact size and α.

$$\alpha = \alpha_1 (N^+_{area})^{\alpha_2} + \alpha_3 \tag{4.2}$$

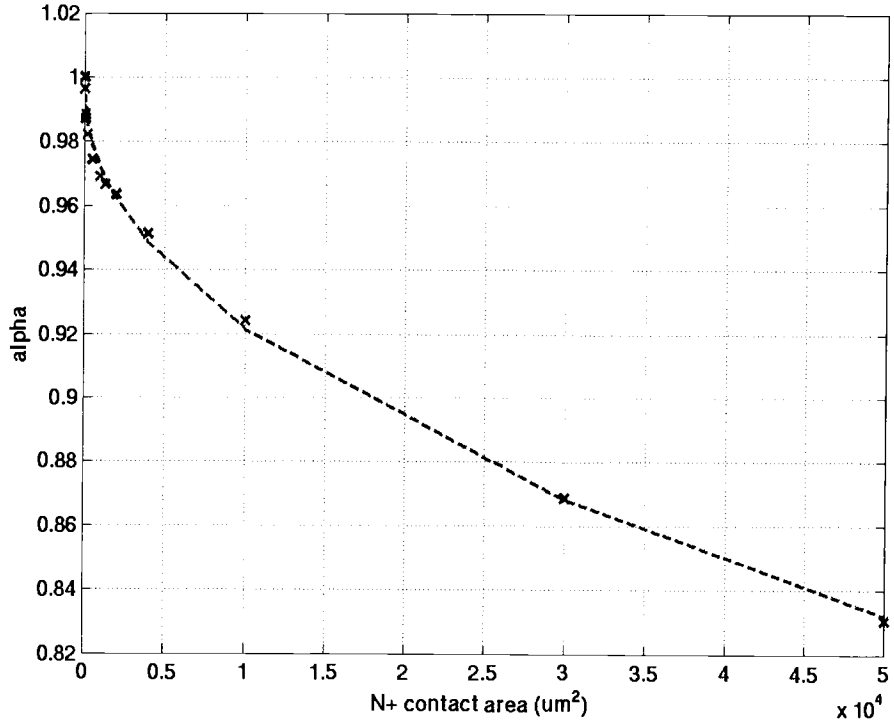

Figure 4-9 α as a function of the N+ contact size. This relationship is described in Equation (4.2). As the N+ contact size increases, α decreases.

Figure 4-10 shows the relationship of β and the N+ contact size. When the N+ contact area is extremely small, the virtual separation is equal to the actual separation. Hence, β is equal to 0 for a small N+ contact. As the N+ contact area increases, β increases. Equation (4.3) describes the relationship of β and the N+ contact size.

$$\beta = \beta_1 (N^+_{area})^{\beta_2} \tag{4.3}$$

Equation (4.1) can now be rewritten as Equation (4.4), the virtual separation equation. Based on the physical difference between N-P and P-P couplings, the virtual separation is larger than or equal to the actual separation.

$$\begin{cases} Virtual\_Separation = (\alpha_1 (N^+_{area})^{\alpha_2} + \alpha_3) Actual\_Separation + \beta_1 (N^+_{area})^{\beta_2} \\ Virtual\_Separation \geq Actual\_Separation \end{cases} \tag{4.4}$$

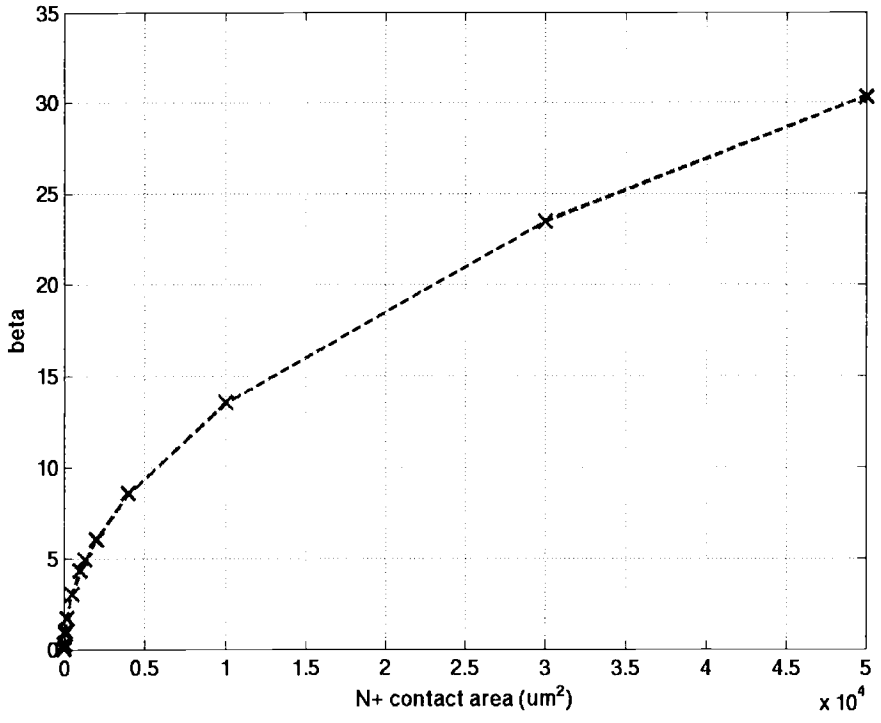

Figure 4-10 β as a function of the N+ contact area. This relationship is described in Equation (4.3). As the N+ contact area increases, β increases.

4.1.3 N-P Test Structures Required for Extracting Parameters for the Virtual Separation Equation

The linear relationship of the virtual and actual separation indicates that there are at least two different separations required in the N-P test structure. The α

and β in Equation (4.4) have parabolic relationships with N+ contact size. Hence, there are at least three different N+ contact sizes required in the N-P structure. In total, six N-P test structures are needed to extract the parameters for the virtual separation equation. The following sections demonstrate the N-P modeling results obtained from both 2-D and 3-D simulations. The virtual separation equation is extracted from six pairs of N-P structures.

4.2 Virtual Separation Verification with 2-D Medici Simulations

In this section, symmetric N+/P+ contacts are simulated. The area of the contact in 2-D simulations is considered to be the square of the contact width. The six pairs of N-P test structures used to construct the virtual separation equation are summarized in Table 4-1.

Table 4-1 The six N-P structures used to construct the virtual separation equation in 2D Medici simulations.

	Contact Width (μm)	Separation (μm)
1st pair	1	1
2nd pair	10	1
3rd pair	31.6	1
4th pair	1	25
5th pair	10	25
6th pair	31.6	25

Simulation results of N-P structures of symmetric contacts of sizes 30μm and 45μm are summarized in Table 4-2 and Table 4-3, respectively. It is observed that a larger virtual separation is needed for a smaller actual separation and the percentage error after applying the virtual separation is significantly improved. At a

large actual separation, the virtual separation approaches the actual separation and the P-P model can describe the N-P coupling.

Table 4-2 Medici simulation results of z_{12NP} modeling for symmetric N-P structures of contact size 30μm. The percentage error is significantly improved especially at small separations.

Actual separation (μm)	Virtual separation (μm)	z_{12NP} (Ω)	$z_{12PPvirtual}$		$z_{12PPactual}$	
			Value (Ω)	Error (%)	Value (Ω)	Error(%)
1	5.46	29.7	28.89	0.6	50.4	69.7
5	9.22	21.8	21.13	-3	31.4	44
10	13.92	14.8	14.36	-3	19.6	32
15	18.63	10.2	9.9	-3	12.9	26.4
20	23.33	7.1	7.01	-1.2	8.7	22.5
25	28.03	5.1	5.09	-0.2	6.1	19.6
30	32.74	3.7	3.8	2.7	4.4	19
35	37.44	2.8	2.92	4.2	3.3	17.8
40	42.15	2.2	2.32	5.4	2.5	13.6
45	46.85	1.9	1.92	1	2.1	10.5
50	51.55	1.6	1.64	2.5	1.72	7.59

Table 4-3 Medici simulation results of modeling z_{12NP} for symmetric N-P structures of contact size 45μm. The percentage error is significantly improved especially at small separations.

Actual separation (μm)	Virtual separation (μm)	z_{12NP} (Ω)	$z_{12PPvirtual}$		$z_{12PPactual}$	
			Value (Ω)	Error (%)	Value (Ω)	Error(%)
1	8.2	11.53	10.6	-8.7	24.8	115
5	11.89	8.59	7.75	-9.7	14.7	71
10	16.51	5.9	5.38	-8.8	8.9	51
15	21.13	4.15	3.86	-6.9	5.9	42
20	25.75	2.99	2.83	-5.3	4.1	37
25	30.37	2.22	2.16	-2.7	2.9	30.6
30	34.99	1.71	1.69	-1.1	2.2	28.6
35	39.6	1.37	1.38	-0.7	1.7	24
40	44.22	1.14	1.16	1.7	1.3	14
45	48.84	0.99	1.01	2	1.1	8.9
50	53.46	0.89	0.9	1.1	0.97	8.9

4.3 Virtual Separation Verification with 3-D Taurus Simulations

2-D simulations can be used only for problems of two symmetric contacts such as the N-P and P-P structures shown in Figure 4-1. However, the substrate coupling is in fact a three-dimensional problem. A N-P model capable of addressing three-dimensional problems is needed. Simulations are performed using the three-dimensional device level simulator, Taurus [16].

The purpose of performing Taurus simulations is to validate the virtual separation concept for unsymmetrical N-P structures. To construct the virtual

separation equation in Taurus simulations, six pairs of symmetric N-P structures are used and their geometries are summarized in Table 4-4. For symmetric N-P structures, Table 4-5, Table 4-6, and Table 4-7 present the N-P modeling results obtained by applying the virtual separation to the equivalent P-P structures.

Table 4-4 The six N-P structures used to construct the virtual separation equation in 3D Taurus simulations.

	Contact Side Length (μm)	Separation (μm)
1st pair	2	2
2nd pair	5	2
3rd pair	15	2
4th pair	2	14
5th pair	5	14
6th pair	15	14

Table 4-5 Taurus simulation results of modeling z_{12NP} for symmetric N-P structures of contact size 5μm x 5μm.

Actual separation (μm)	Virtual separation (μm)	z_{12NP} (Ω)	$z_{12PPvirtual}$		$z_{12PPactual}$	
			Value (Ω)	Error (%)	Value (Ω)	Error(%)
2	2.93	121	126	4	156	29
6	6.73	76.8	72.72	-5.3	83.6	9.2
10	10.54	45.8	44.6	-2.6	48.4	5.6
14	14.35	27.9	28.35	1.6	29.3	5

Table 4-6 Taurus simulation results of modeling z_{12NP} for symmetric N-P structures of contact size 10μm x 10μm.

Actual separation (μm)	Virtual separation (μm)	z_{12NP} (Ω)	$z_{12PPvirtual}$		$z_{12PPactual}$	
			Value (Ω)	Error (%)	Value (Ω)	Error(%)
2	4	60.6	68.1	12	92.6	36
6	7.68	41.9	41.98	0.2	52.4	25
10	11.35	26.8	26.35	-1.6	31.9	19
14	15	16.6	17.6	6	19.5	17

Table 4-7 Taurus simulation results of modeling z_{12NP} for symmetric N-P stuctures of contact size 15μm x 15μm.

Actual separation (μm)	Virtual separation (μm)	z_{12NP} (Ω)	$z_{12PPvirtual}$		$z_{12PPactual}$	
			Value (Ω)	Error (%)	Value (Ω)	Error(%)
2	5.13	39.9	40.48	1.4	66.5	66
6	8.71	28.7	25.9	4.1	37.7	31
10	12.3	18.2	16.9	-7	22.6	24
14	15.88	11.8	11.88	0.6	14.3	21

The unsymmetrical N-P coupling simulations can be performed in Taurus to validate the virtual separation concept. To apply the virtual separation for the unsymmetrical N-P coupling, the actual separation is stretched in the direction of the largest distance between the two contacts. Here, three examples are demonstrated and are shown in Figure 4-11. Their simulation results are shown in Table 4-8.

Table 4-8 Taurus simulation results of modeling three nonsymmetrical N-P structures by applying virtual separations to equivalent P-P structures.

	Z_{12NP} (Ω)	$Z_{12PPvirtual}$		$Z_{12PPactual}$	
		Value (Ω)	Error (%)	Value (Ω)	Error (%)
Figure 4-10(a) left	66.5	69.3	4	95.2	43
Figure 4-10(a) right	65	63.7	-2	84	29
Figure 4-10(b)	62.5	60.7	-3	75.7	21

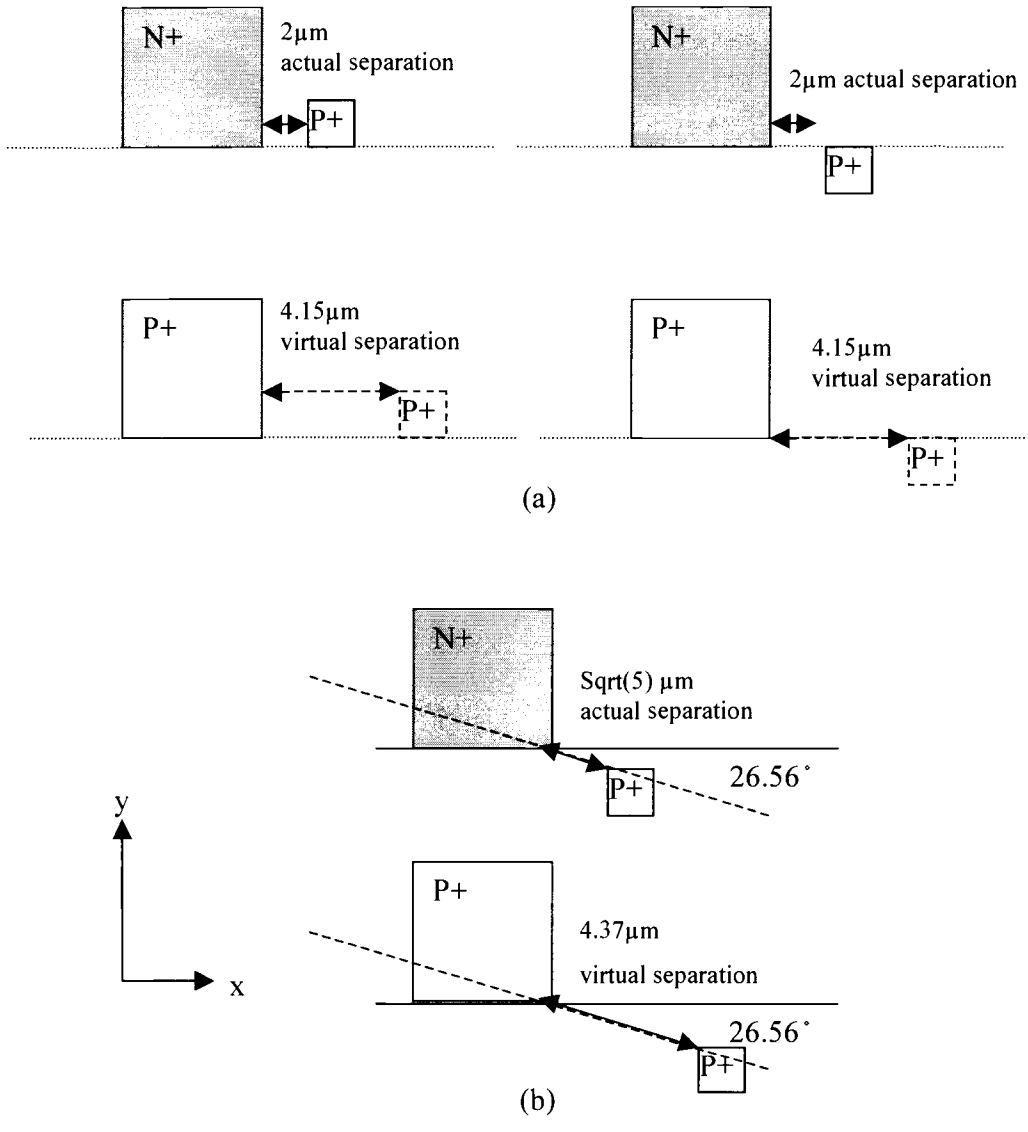

Figure 4-11 Unsymmetrical N-P coupling structures in 3D Taurus simulations. The N+ contact is 15μm x 15μm and the P+ contact is 2μm x 2μm. (a) The nonsymmetrical N+ and P+ contacts are aligned on the x-axis. Hence, the virtual separation is stretched in the x direction. (b) The largest distance between the nonsymmetrical N+/P+ contacts is marked with an arrow. The virtual separation is stretched in the direction of the arrow.

4.4 Summary

In this chapter, a new N-P model is developed by taking advantage of an existing P-P model and the concept of a virtual separation. An equation for the virtual separation is established. The virtual separation equation requires five parameters that can be extracted from a minimum number of six pairs of N-P structures. The virtual separation concept is verified using both 2D and 3D simulations.

5 VALIDATIONS OF N-P MODEL WITH MEASURED DATA

Measurement of the coupling in N-P structures is more challenging than DC measurements for P-P structures. In the N-P structure, there is a junction capacitor which is an open circuit at DC. This junction capacitance is in the range of femto farads, which is a lot smaller than that of most of the commercial probes. Hence, direct measurement of the coupling in the N-P structure is a challenging task. A pseudo-inverter structure was proposed in [17] as a simple technique to extract interconnect capacitances in sub femto-farad ranges. The pseudo-inverter structure leads to the possibility for extracting the resistances and the capacitance of the N-P structure with the convenience of DC current measurements. However, further investigation is needed to resolve some physical feasibility issues. In this work, DC measurements of test structures in [18] are used.

The test structures of [18] are fabricated in a 0.35μm TSMC CMOS heavily doped process. An EPIC [11] calibrated profile of the same process is available in [13]. Hence, the resistance between the N+ and P+ contacts can be extracted by the DC measurements and Epic simulation results.

According to Section 4.1.3, six N-P test structures including three different N+ sizes and two different separations are required to construct the virtual separation equation. In this chapter, the parameters of the equation are extracted from measured data for six single-finger transistor structures. Six other single-finger transistor structures and 4 four-finger transistor structures are used for verification purposes.

5.1 Single-Finger Test Structure for Constructing and Validating the Virtual Separation Equation

The single finger structure in [18] is shown in Figure 5-1 with contacts 2, 3, and 4 connected as node A and contacts 1 and 5 connected as node B. The resistance is measured between nodes A and B. The single finger structure can be viewed as a 5-contact structure. Since contacts 2, 3 and 4 are right next to each other, R_{23} and R_{34} are fairly small and can be ignored. As a result, R_{22} is in parallel with R_{33} and R_{33} is in parallel with R_{44}. Hence, R_{24} can be ignored. R_{25} is fairly large compared with R_{12} because for R_{25} there are two contacts between contacts 2 and 5. R_{14} is fairly large compared with R_{45} for the same reason. Hence, the cross coupling resistance will be the parallel combination of R_{12}, R_{45}, R_{13} and R_{35}. R_{12} and R_{45} are the resistances between the N+ and P+ contacts and will be extracted. Since the structure is symmetric, R_{12} and R_{45} are identical in their values. For extracting the virtual separation equation, six single finger structures are required and these are summarized in Table 5-1.

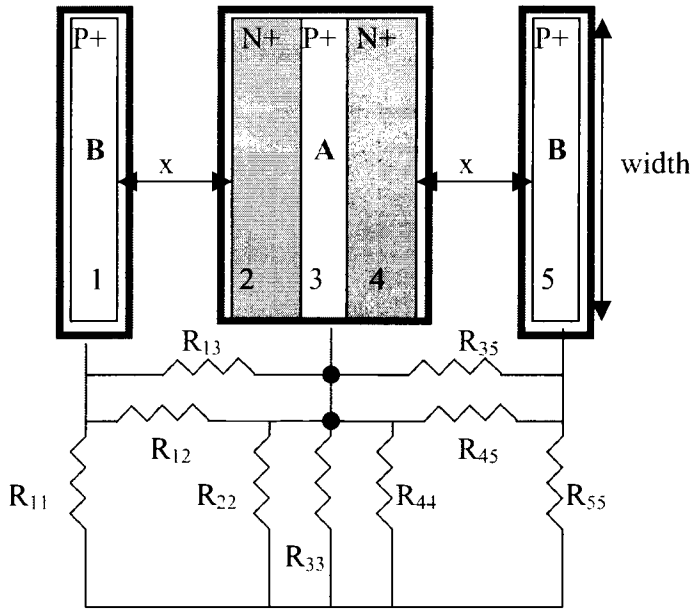

Figure 5-1 A single finger structure.

Table 5-1 6 single finger structures used for extracting parameters of the virtual separation equation from measurements.

	x (μm)	width (μm)
1st single finger structure	2	25
2nd single finger structure	2	25
3rd single finger structure	2	50
4th single finger structure	3	50
5th single finger structure	3	200
6th single finger structure	3	200

The virtual separation is plotted as a function of the actual separation in Figure 5-2. The solid line of slope of 1 in this figure is obtained from the observation that an extremely small N+ contact acts like a P+ contact. In the shaded region (Figure 5-2), the actual separation is larger than the extra distance carriers travel in the N-P structure. Hence, the virtual separation is equal to the actual separation and the P-P model can directly model the N-P coupling. The slopes (α) and y-intercepts (β) of the dashed lines are dependent on the size of the N+ contact. Equations (4.2) and (4.3) are used to curve fit α and β parameters in Figure 5-3 and Figure 5-4, respectively. These empirical parameters are summarized in Table 5-2 and the modeling results are summarized in Table 5-3.

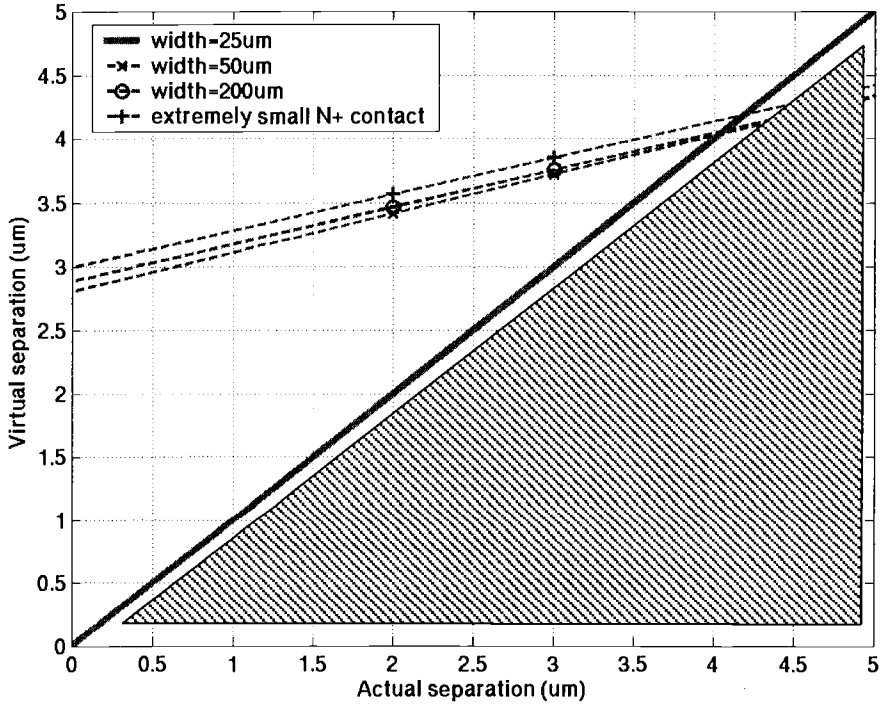

Figure 5-2 Virtual separation as a function of actual separation. The solid curve indicates that an extremely small N+ contact acts like a P+ contact. The shaded region indicates that the P-P model can be applied to N-P coupling without the use of a virtual separation.

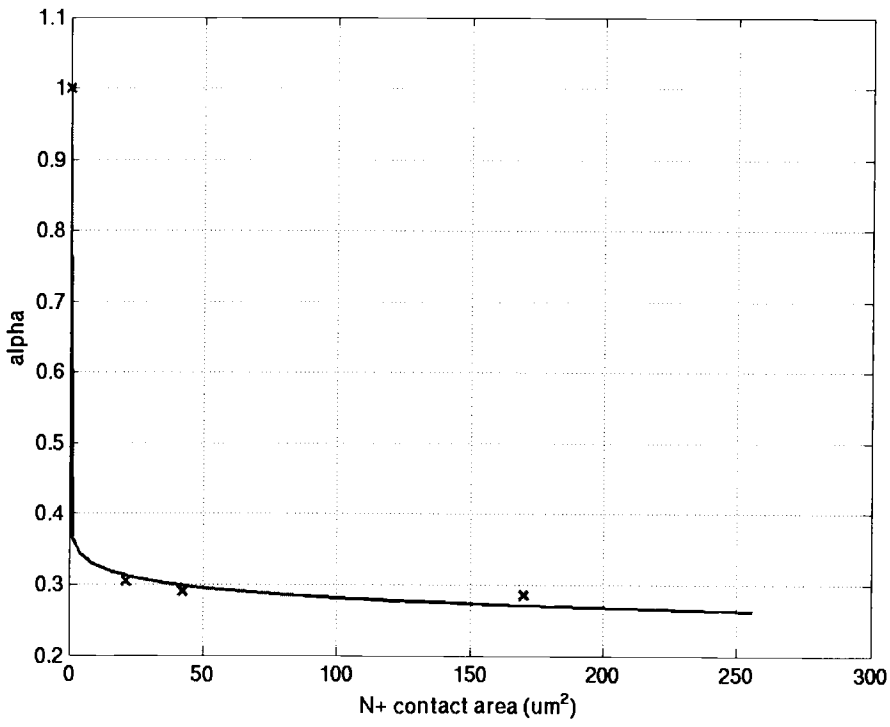

Figure 5-3 α as a function of the N+ contact size. The curve fit of Equation (4.2) is also shown (solid line).

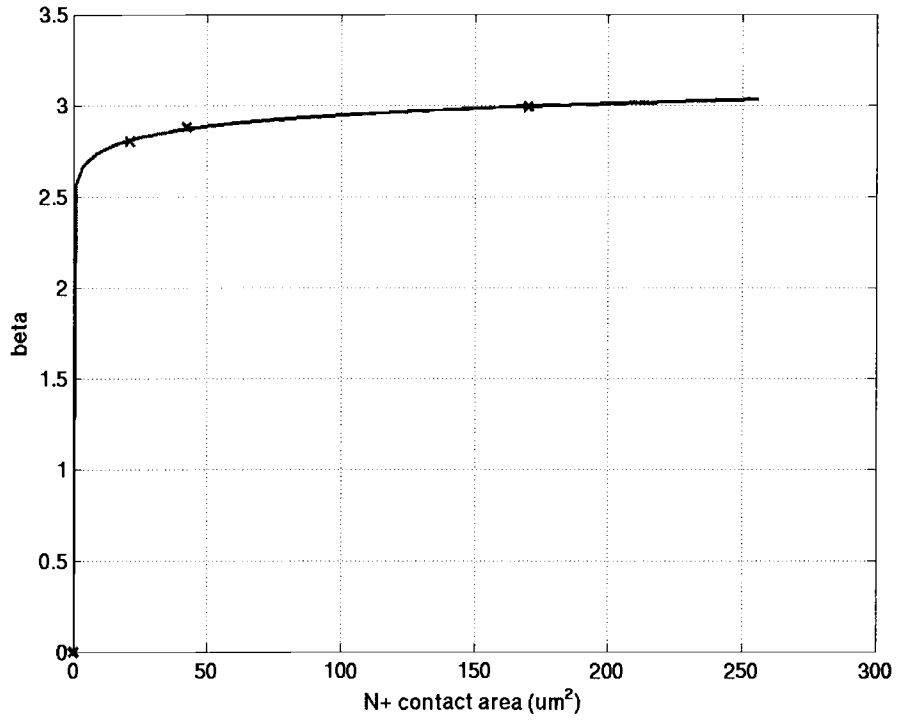

Figure 5-4 β as a function of N+ contact size. The curve fit of Equation (4.3) is also shown (solid line).

Table 5-2 Extracted α and β parameters.

α	α_1	-0.6309
	α_2	0.028
	α_3	0.9991
β	β_1	2.5637
	β_2	0.0303

Table 5-3 N-P modeling results from measurements. The numbers in bold are the data used for extracting the parameters for the virtual separation equation.

Width = 25 μm				
Actual separation (μm)	Virtual separation (μm)	R_{NP} (Ω)	$R_{PPvirtual}$	
			Value (Ω)	Error (%)
2um	**3.4um**	**561**	**560**	**-0.1**
2.5um	3.59um	585	594	1.5
3um	**3.72um**	**603**	**600**	**-0.5**
3.5um	3.9um	654	627	-4
Width = 50 μm				
Actual separation (μm)	Virtual separation (μm)	R_{NP} (Ω)	$R_{PPvirtual}$	
			Value (Ω)	Error (%)
2um	**3.45um**	**284**	**283**	**-0.4**
2.5um	3.61um	294	298	1.3
3um	**3.76um**	**307**	**307**	**0**
3.5um	3.91um	321	314	-2
Width = 200 μm				
Actual separation (μm)	Virtual separation (μm)	R_{NP} (Ω)	$R_{PPvirtual}$	
			Value (Ω)	Error (%)
2um	**3.55um**	**73**	**73**	**0**
2.5um	3.67um	75	75	0
3um	**3.85um**	**78**	**78**	**0**
3.5um	3.95	85	80	-6

Table 5-3 shows that a larger N+ contact requires a larger virtual separation. A similar phenomenon is observed from the simulated results presented in Chapter 4.

5.2 Four-Finger Test Structure for Validating the Virtual Separation Equation

The virtual separation equation obtained in Section 5.1 is used to compute the resistance values of 4 four-finger test structures. The computed resistance is compared against the measured value to verify the virtual separation equation.

The 4-finger structure is shown in Figure 5-5 where the shaded regions are the N+ contacts and the white regions are the P+ contacts. The width of the structure is 25μm. Contacts 2 to 10 are connected as node A and contacts 1 and 11 are connected as node B. The resistance is measured between nodes A and B. Table 5-4 lists the results of the measured resistance and the computed resistance using the new N-P model. The detailed information of the computed resistance is shown in Appendix B.

For x of 2μm, the resistance value computed using the N-P model agrees with the measured resistance value. For x larger than 5μm, the virtual separation from the N-P model is equal to the actual separation, which means that the distance of 5μm is large enough to weaken the effect of the N+ contact. Hence, the P-P model can be applied directly.

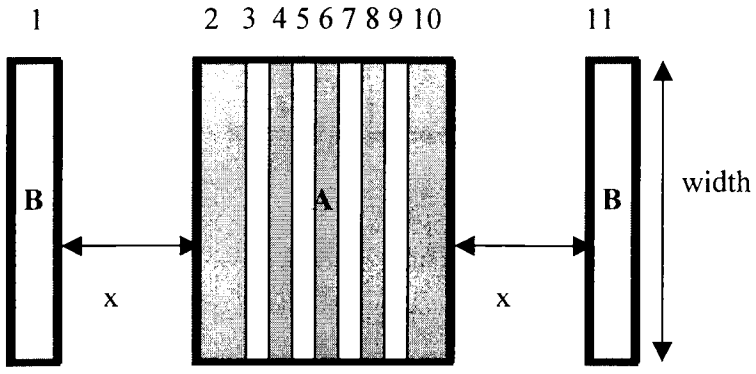

Figure 5-5 A 4-finger test structure. The shaded areas are the N+ contacts and the white areas are the P+ contacts. The width is 25 μm.

Table 5-4 The measured resistance, the computed resistance using the N-P model, and the computed resistance using the N-P model.

	x = 2 μm	x = 5 μm	x = 8 μm	x = 12 μm
Measured Resistance (Ω)	171	216	262	322
Computed Resistance using the N-P model (Ω)	170.4	217	272	333
Computed Resistance using the P-P model (Ω)	124	217	272	333

5.3 Summary

The parameters of the virtual separation equation are extracted by using six measurements of single-finger transistor structures fabricated in a 0.35μm TSMC CMOS heavily doped process. The virtual separation equation is successfully validated with both single and four finger transistor test structures.

6 APPLICATIONS OF THE NEW N-P MODEL

A three-stage ring oscillator circuit is used as an example to demonstrate the need for an N-P model. The virtual separation equation obtained from Chapter 5 is used to compute the substrate resistive network between the N+ and P+ contacts. In this example, the use of the N-P model and the P-P model shows a significant difference when the backplane is grounded. This example is presented in Section 6.1.

A structure made up of one N+ injector and ten P+ sensors of different sizes is simulated at 100MHz both with the N-P model and the P-P model, respectively. The resistive substrate network is more complicated for this structure and noise sensed at the sensor depends on the current distribution in the network. This example is shown in Section 6.2.

6.1 A Three-Stage Ring Oscillator Circuit

A three-stage ring oscillator circuit (Figure 6-1) is used with each inverter of the same size. The PMOS transistor is of size 200μm/0.35μm and the NMOS transistor is of size 100μm/0.35μm. The BSIM3 transistor model for the TSMC 0.35μm process is used. The ring oscillator oscillates at approximately 555 MHz. Since the PMOS transistor resides in a N-well, the NMOS transistor switching noise dominates. Hence, only three NMOS transistors are used in the layout. Figure 6-2 shows the layout of these three NMOS transistors. There are two sensors in this circuit. The first sensor is a 15μm x 0.7μm grounded P+ substrate tap for measuring the noise current in the substrate. The second sensor is a 20μm x 20μm floating P+ diffusion region for sensing the noise voltage at this location. Both sensors are placed 2μm apart from these three transistors. The three NMOS transistors are laid out as 2-finger SDS (Source/Drain/Source) structures. The

arrows in Figure 6-2 indicate where the concept of virtual separation needs to be applied.

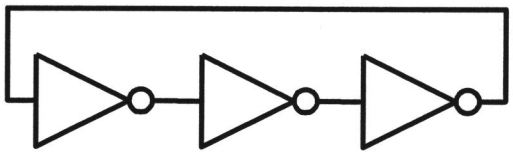

Figure 6-1 A three-stage ring oscillator circuit.

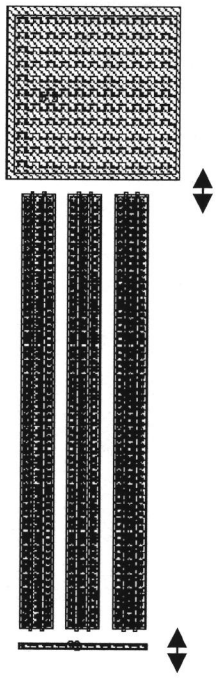

Figure 6-2 Layout of three NMOS transistors in the 3-stage ring oscillator circuit. The arrows indicate where virtual separations need to be used.

6.1.1 Resistive Substrate Network for the Circuit Example

The source, drain, and source regions in each of the three NMOS transistors, the P+ grounded sensor, and the P+ floating sensor form a structure of 11 contacts. To compute the P-P model, this structure of 11 P+ contacts with actual separations is simulated in EPIC. To compute the N-P model, the structure of 11 P+ contacts with virtual separations is simulated in EPIC. Based on the virtual separation equation, the P+ taps should be placed at 3.47μm away from the NMOS transistors to accurately compute the cross coupling resistance values.

In Chapter 2, the drain region of the NMOS transistor was identified to be the effective noise injection area of an inverter and the substrate network connections at the circuit level were validated. Hence, in this chapter, the substrate resistive network is a network of 5 contacts formed between the three drain regions and the two P+ sensors.

6.1.2 Simulation Results

In this section, simulations of the 3-stage ring oscillator for both floating and grounded backplanes are compared. Here, a simplified substrate resistive network made up of one injector, one grounded sensor, and one floating sensor is used to explain the cases of a floating and a grounded backplanes. The resistance values are obtained from the computed P-P and N-P models.

When the backplane is floating in Figure 6-3, there is only one ground, the grounded sensor, in the circuit. Even though the N-P model has the more resistive paths 1 and 3 than the P-P model, the noise current eventually propagates to the grounded sensor. Hence, the substrate noise current simulation results obtained with the N-P model are similar to the simulation results obtained with the P-P model. The larger cross-coupling resistances in the N-P model have an insignificant effect on the sensed noise voltage at the floating sensor. Hence, the noise voltage simulation results are similar with either the N-P or the P-P models.

However, when the backplane is grounded as in Figure 6-4, approximately 40% more of the noise current propagates through path 1 and approximately 24% more of the noise current propagates through path 3 in the P-P model than in the N-P model. Hence, the sensors pick up less noise in the N-P model than in the P-P model.

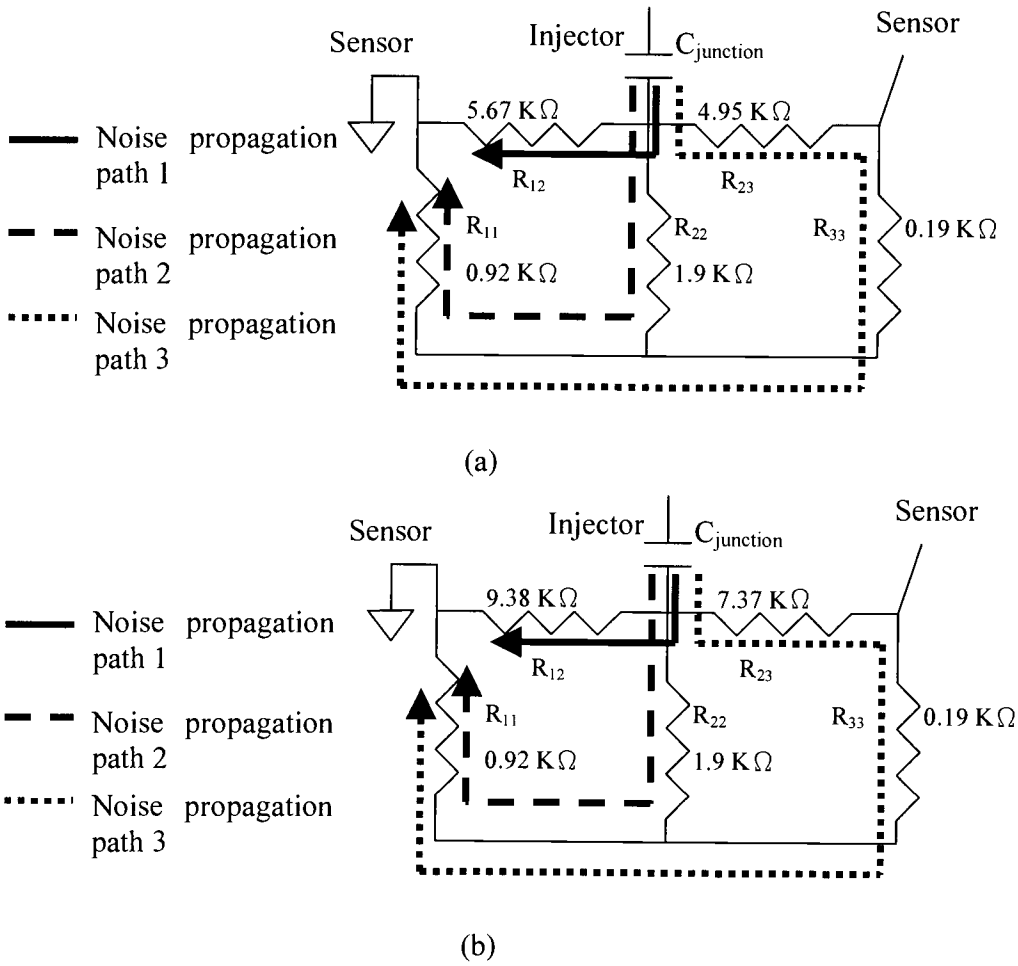

Figure 6-3 Resistive substrate network with a floating backplane. (a) The P-P model. (b) The N-P model.

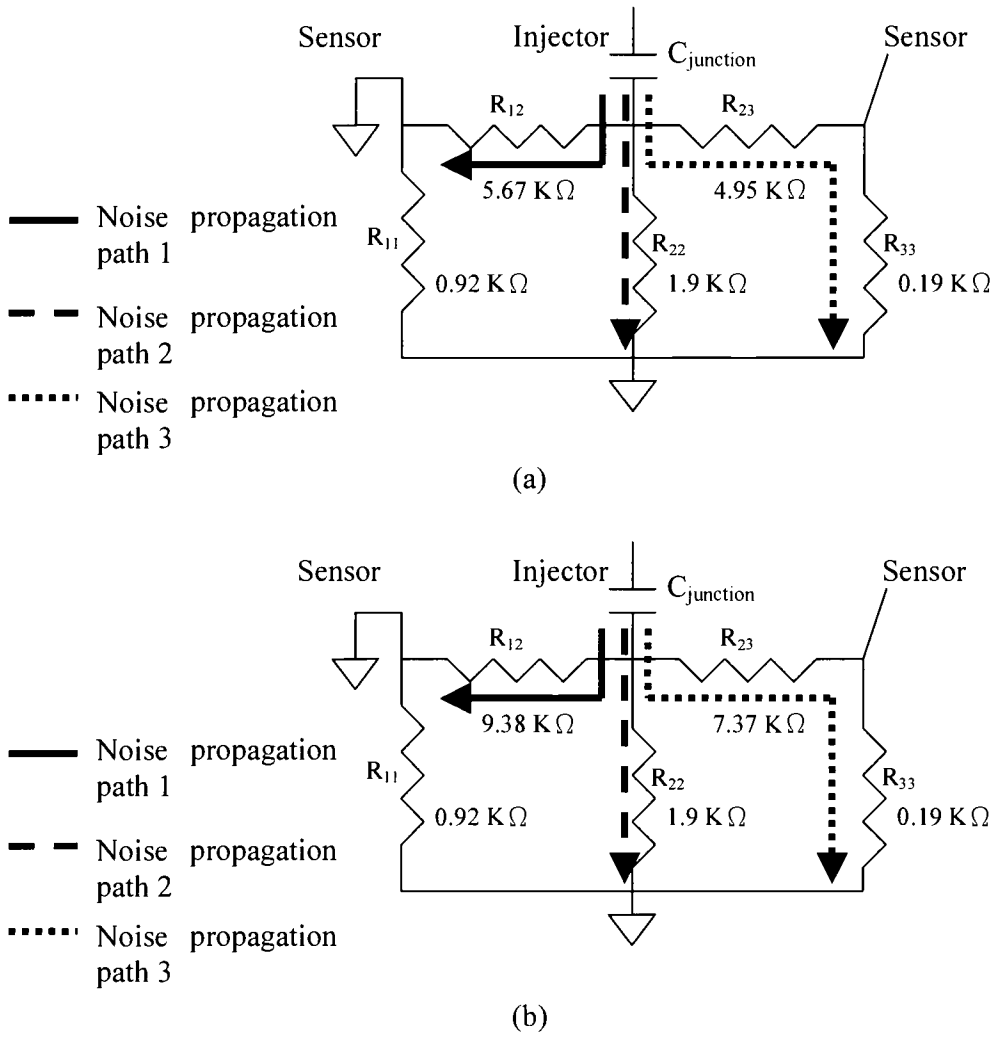

Figure 6-4 Substrate resistive network with a grounded backplane. (a) The P-P model. (b) The N-P model.

6.1.2.1 Simulation Results with a Floating Backplane

Figure 6-5 shows the transient noise current waveform picked up at the grounded small P+ substrate tap next to the NMOS transistors. In the simulation with the P-P model, the 15μm x 0.7μm grounded P+ tap picks up a peak-to-peak noise current of 62.75 μA. In the simulation with the N-P model, the grounded P+ tap picks up a peak-to-peak noise current of 54.87 μA. The difference is approximately 14 %.

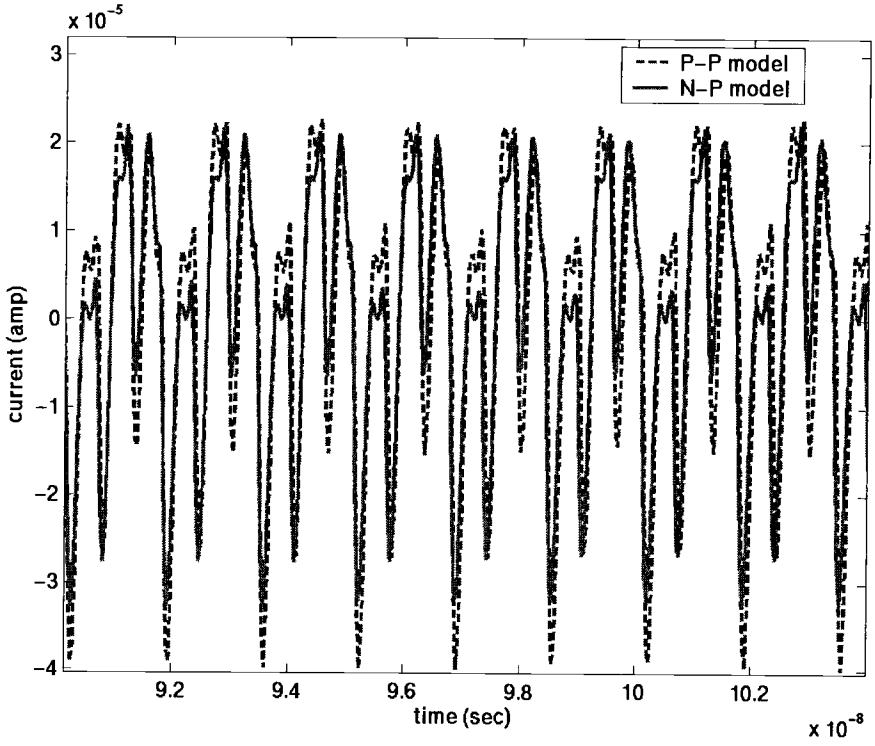

Figure 6-5 Simulated noise current waveform picked up at the grounded 15μm x 0.7μm P+ substrate tap with the backplane floating.

Figure 6-6 shows the noise voltage waveform sensed at the floating 20μm x 20μm P+ sensor. In the simulation with the P-P model, the sensor senses a peak-to-

peak noise voltage of 40.8 mV. With the N-P model, the sensor senses a peak-to-peak noise voltage of 37.2 mV. The difference is approximately 9.7 %.

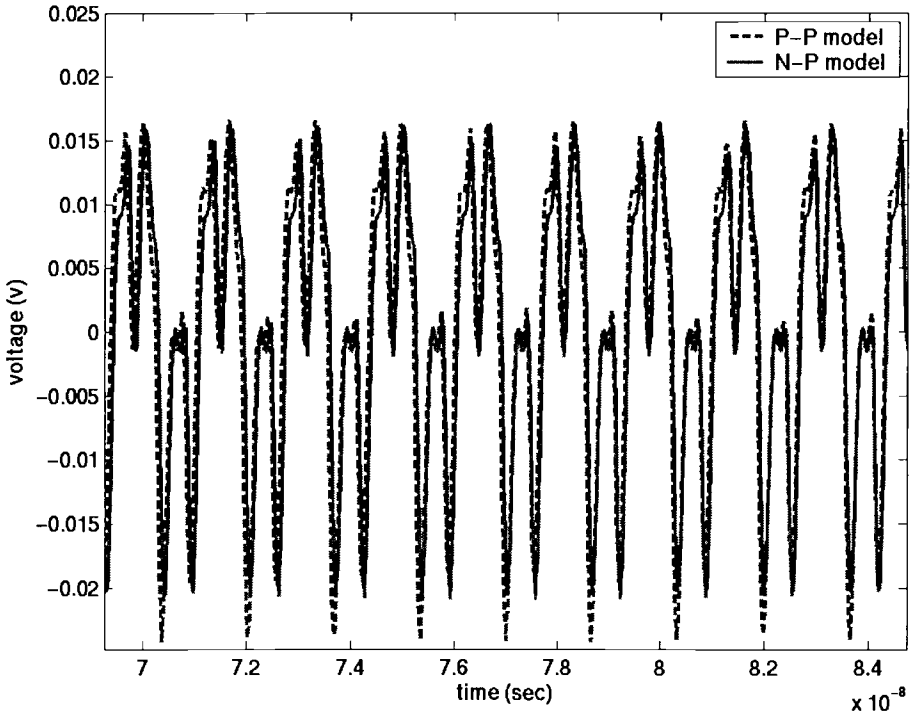

Figure 6-6 Simulated noise voltage waveform sensed at the floating 20μm x 20μm P+ sensor with the backplane floating.

6.1.2.2 Simulation Results with a Grounded Backplane

Figure 6-7 shows the noise current transient waveform picked up at the grounded 15μm x 0.7μm P+ tap. The simulation result obtained with the P-P model shows a peak-to-peak noise current of 33.07 μA. The simulation result obtained

with the N-P model shows a peak-to-peak noise current of 19.99 μA. The difference is as much as 65.4 %.

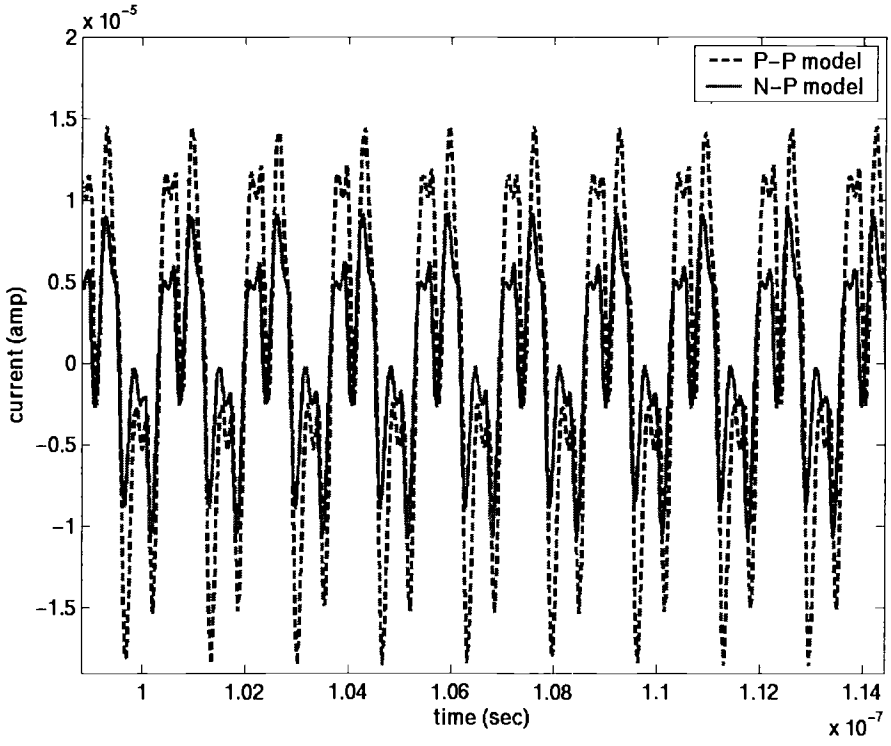

Figure 6-7 Simulated noise current waveform picked up at the grounded P+ substrate tap with the backplane grounded.

Figure 6-8 shows the noise voltage sensed at the floating 20μm x 20μm P+ sensor located 2μm apart from the NMOS transistors. With the P-P model, the sensor senses a peak-to-peak noise voltage of 6.9 mV. With the N-P model the sensor senses a peak-to-peak noise voltage of 5.3 mV. The difference is approximately 31 %.

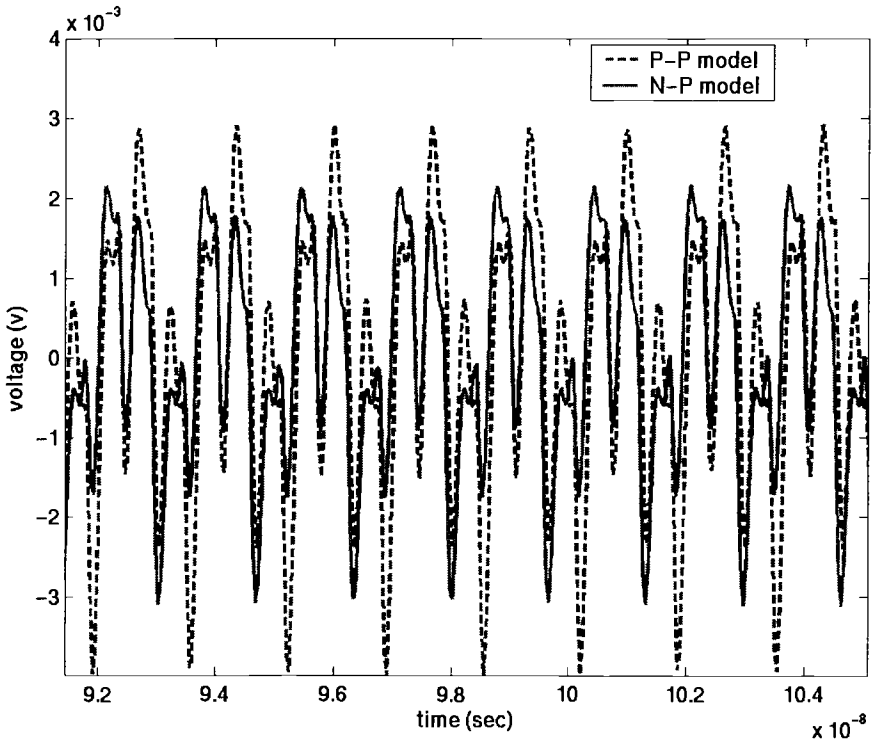

Figure 6-8 Simulated noise voltage waveform sensed at the floating 20μm x 20μm P+ sensor with the backplane grounded.

When the backplane is grounded, the use of the N-P model in substrate noise coupling simulations is more important. The simulated noise current waveforms show a difference of 60% between the two models while the simulated voltage waveforms show a difference of 30% between the two models. Here, the resistance values in Figure 6-4 are used to explain this large error difference.

In Figure 6-4, the R_{23NP} is scaled from the R_{23PP} with a scaling factor of λ as in Equation (6-1). The R_{12NP} is scaled from the R_{12PP} with a different scaling factor of γ as in Equation (6-2). λ and γ differ in value due to the different sizes of the two P+ diffusion regions. The mathematical equations of the sensed noise current and the sensed noise voltage are represented in Equations (6.3) and (6.4). As a result,

the percentage errors of the I_{NP} and V_{NP} computed with Equations (6.5) and (6.6) respectively are different.

$$\lambda = \frac{R_{23NP}}{R_{23PP}} > 1 \tag{6.1}$$

$$\gamma = \frac{R_{12NP}}{R_{12PP}} > 1 \tag{6.2}$$

$$I_{NP} = \frac{R_{22PP}(\lambda R_{23PP} + R_{33PP})}{\gamma R_{12PP}(R_{22PP} + \lambda R_{23PP} + R_{33PP}) + R_{22PP}(\lambda R_{23PP} + R_{33PP})} \tag{6.3}$$

$$V_{NP} = \frac{R_{22PP}\gamma R_{12PP} R_{33}}{\gamma R_{12PP}(R_{22PP} + \lambda R_{23PP} + R_{33PP}) + R_{22PP}(\lambda R_{23PP} + R_{33PP})} \tag{6.4}$$

$$I_{PP} = \frac{R_{22PP}(R_{23PP} + R_{33PP})}{R_{12PP}(R_{22PP} + R_{23PP} + R_{33PP}) + R_{22PP}(R_{23PP} + R_{33PP})} \tag{6.5}$$

$$V_{PP} = \frac{R_{22PP} R_{12PP} R_{33}}{R_{12PP}(R_{22PP} + R_{23PP} + R_{33PP}) + R_{22PP}(R_{23PP} + R_{33PP})} \tag{6.6}$$

6.2 Multiple Sensor Example

Section 6.1 demonstrated a circuit example with only one grounded sensor and one floating sensor. Simulations of this example showed a greater difference between the N-P and P-P models when the backplane is grounded. In this section, a resistive substrate network made up of one N+ injector and ten P+ sensors of different sizes is shown in Figure 6-9. The sizes of the contacts range from 2μm x 2μm to 20μm x 20μm. Contacts 2, 3, 10, and 11 are floating sensors and contacts 4 to 9 are grounded sensors. Contacts 2, 4, 6, 8, and 10 are placed 5μm from the injector and contacts 3, 5, 7, 9, and 11 are placed 2μm from the injector. The P-P model is obtained from this structure with actual separations. For the N-P model, virtual separations of 3.47μm are used for contacts (3, 5, 7, 9, and 11) that are placed 2μm from the injector. For each model, the resistive substrate network with a junction capacitor at the N+ injector is simulated at 100MHz for both floating and

grounded backplanes. An AC small signal voltage is placed at the N+ injector in simulations.

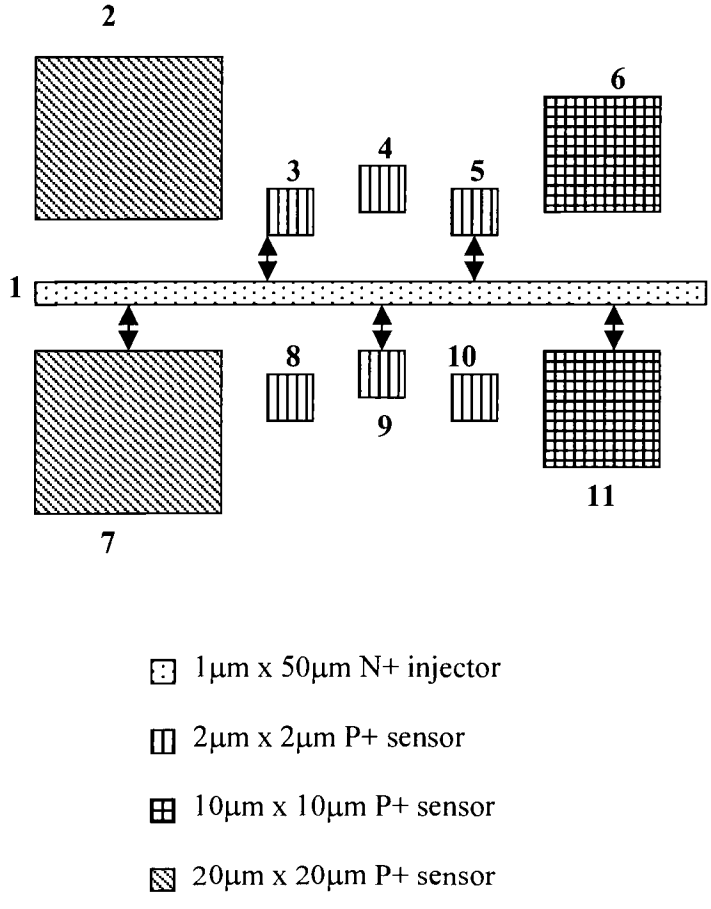

Figure 6-9 An example with 11 contacts; 1 N+ injector and 10 P+ sensors of different sizes. Contacts 2, 3, 10, and 11 are floating sensors. Contacts 4 to 9 are grounded sensors. The arrows indicate where the virtual separation is needed.

Table 6-1 Voltage and current magnitudes sensed from the sensors in Figure 6-9 with the backplane floating.

	P-P model	N-P model	Error (%)
Voltage magnitude at contact 2	7.76mV	9.22mV	-15.8
Voltage magnitude at contact 3	9.13mV	9.24mV	-1
Voltage magnitude at contact 10	7.63mV	8.29mV	-7.9
Voltage magnitude at contact 11	9.28mV	9.76mV	-5
Current magnitude at contact 4	8.42μA	9.65μA	-12.7
Current magnitude at contact 5	11.26μA	9.19μA	22.5
Current magnitude at contact 6	27.32μA	32.87μA	-16.8
Current magnitude at contact 7	63.62μA	59.96μA	6.1
Current magnitude at contact 8	3.99μA	4.71μA	-15.2
Current magnitude at contact 9	11μA	9.23μA	19

Table 6-1 summarizes the simulation results with a floating backplane. Noise current from the N+ injector is distributed depending on the value of each resistor in this network. As a result, the percentage errors between the N-P model and the P-P model show a greater difference at a few sensors but show a smaller difference at other sensors. For example, contact 5 senses a noise current magnitude of 11.26μA with the P-P model and a noise current magnitude of 9.19μA with the N-P model. Their difference is 22.5%. At contact 3, the difference between the two models is only -1%.

Table 6-2 Voltage and current magnitudes sensed from the sensors in Figure 6-9 with the backplane grounded.

	P-P model	N-P model	Error (%)
Voltage magnitude at contact 2	3.55mV	4.2mV	-15
Voltage magnitude at contact 3	6.76mV	6.32mV	7
Voltage magnitude at contact 10	4.72mV	4.64mV	1.7
Voltage magnitude at contact 11	5.69mV	5.22mV	9
Current magnitude at contact 4	5.6μA	6.21μA	-10.7
Current magnitude at contact 5	8.65μA	6.57μA	31.6
Current magnitude at contact 6	14.83μA	17.89μA	-17
Current magnitude at contact 7	32.44μA	25μA	29.7
Current magnitude at contact 8	2.57μA	2.97μA	-13.4
Current magnitude at contact 9	8.2μA	6.27μA	30.7

Table 6-2 summarizes the simulation results with a grounded backplane. For either the N-P model or the P-P model, the noise current is distributed depending on the resistor values in the network. As a result, for a few sensors the difference between the two models is small, whereas for other sensors a significant difference is observed. For example, contact 5 senses a noise current magnitude of 8.65μA with the P-P model and a noise current magnitude of 6.57μA with the N-P model. The percentage error between the two models for this contact is 31.6%. However, contact 10 senses a noise voltage magnitude of 4.64mV with the N-P model and a noise voltage magnitude of 4.72mV with the P-P model. The percentage error between the two models for this contact is 1.7%.

6.3 Summary

A three-stage ring oscillator with the resistive substrate network computed from the P-P model and the N-P model has been demonstrated. These simulations are done with both floating and grounded backplanes. For a grounded backplane, the simulation results show a significant difference between the P-P model and the N-P model. An N-P model should be used to accurately simulate the substrate noise coupling for this case.

An 11-contact structure (1 N+ injector and 10 P+ sensors) with the resistive substrate network computed from both N-P and P-P models is simulated at 100MHz with both floating and the grounded backplanes. For this structure, noise current distribution is dependent on the resistor values and ground connections in the network. For some sensors, a significant difference is observed between the N-P and P-P model. For other sensors, the difference between the N-P model and the P-P model is small.

7 CONCLUSION AND FUTURE WORK

This thesis focuses on the importance of transistor switching noise for substrate noise coupling. As the package inductance is reduced, this becomes an important coupling mechanism and must be understood and accurately modeled. All the analysis and modeling have been done for heavily doped substrates only.

NMOS transistor noise injection has been analyzed at the device level by studying a digital inverter. The noise injection for the NMOS transistor has been found to be the drain region. Substrate network connections for the NMOS transistor have been identified and verified with device level simulations. The PMOSFET noise injection is less important because the PMOS transistor resides in a N-well.

The coupling between N-P and P-P contacts has been studied extensively at the device level. The self-coupling parameters for N-P structures are similar to those for P-P structures. The cross-coupling parameters of the N-P structures are similar to those of the P-P structures at large separations. However, at short separations, there are significant differences.

A new N-P model has been developed by taking advantage of an existing P-P model combined with the concept of a virtual separation. The virtual separation concept has been validated with 2D/3D simulations and measurements. This model has been validated up to 2GHz with Medici simulations and it should be used for circuit simulations when transistor switching noise is the dominant source of substrate noise.

A three-stage ring oscillator has demonstrated the difference between the use of the N-P and P-P models when transistor switching noise is dominant. For this circuit, the use of the N-P model shows a significant difference from the P-P model when the backplane is grounded. Also, analysis of an 11-contact structure made up of 1 N+ injector and 10 P+ sensors has been performed to examine the difference between the N-P and P-P models. In this structure with multiple

grounded and floating sensors, noise current is distributed according to the resistor values and the ground connections in the substrate network. From these simulation results, the noise current/voltage sensed from a few sensors have shown a significant difference between the N-P and P-P models. Hence, the new N-P model is recommended for circuit simulations when transistor switching noise is the dominant source of substrate noise.

There are three suggestions for future work. The first suggestion is that transistor switching noise needs to be analyzed for a Nand gate circuit where two NMOS transistors are cascoded. This includes investigation of the noise injection area and identification of a substrate network for the circuit. The second suggestion is the development of a N-N model for coupling between N+ contacts. The concept of the virtual separation can possibly be extended for this N-N model. The third suggestion is the investigation of coupling between N+-P+ contacts in lightly doped substrates. For lightly doped substrates, the junction capacitance between a N+ contact and the p-type substrate is less than that in heavily doped substrates. For this reason, the difference between N-P and P-P structures in lightly doped substrates needs to be examined.

BIBLIOGRAPHY

[1] M. van Heijningen, J. Compiet, P. Wambacq, S. Donnay, M. G. E. Engels, and I. Bolsens, "Analysis and experimental verification of digital substrate noise generation for epi-type substrates," *IEEE J. Solid-State Circuits*, vol. 35, pp. 1002 – 1008, July 2000.

[2] S. Adluri, "Contribution to substrate noise due to supply coupling and pin parasitics," M.S Thesis, Oregon State University, 2003.

[3] N. K. Verghese and D. J. Allstot, "Computer-aided design considerations for mixed-signal coupling in RF integrated circuits," *IEEE J. Solid-State Circuits*, vol. 33, pp. 314 – 323, March 1998.

[4] R. Gharpurey and R. G. Meyer, "Modeling and analysis of substrate coupling in integrated circuits," *IEEE J. Solid-State Circuits*, vol. 31, pp. 344 – 353, March 1996.

[5] J. P. Costa, M. Chou and L. M. Silveria, "Efficient techniques for accurate modeling and simulation of substrate coupling in mixed-signal IC's," *IEEE Trans. Computer-Aided Design*, vol. 18, pp. 597 – 607, May 1999.

[6] A. J. van Genderen, N. P. van der Meijs and T. Smedes, "Fast computation of substrate resistances in large circuits," *Proc. European Design and Test Conference*, March 1996, pp. 560 – 565.

[7] A. Samavedam, A. Sadate, K. Mayaram, and T. S. Fiez, "A scalable substrate noise coupling model for design of mixed-signal IC's" *IEEE J. Solid-State Circuits,* vol. 35, pp. 895 – 904, June 2000.

[8] B. Owens, P. Birrer, S. Adluri, R. Shreeve, S. A. Arunachalam, H. Habal, S. Hsu, A. Sharma, K. Mayaram, and T. Fiez, "Strategies for simulation, measurement and suppression of digital noise in mixed-signal circuits," *Proceedings of IEEE Custom Integrated Circuits Conference*, Sept. 2003, pp. 361-364.

[9] E. Schrik, P.M. Dewilde and N.P. van der Meijis, "Theoretical and practical validation of combined BEM/FEM substrate resistance modeling," *ICCAD 2002. IEEE/ACM International Conference*, Nov. 2002, pp. 10-15.

[10] I. L. Wemple and A.T. Yang, "Integrated circuit substrate coupling models based on Voronoi tessellation substrate macromodels," *IEEE Trans. Computer-Aided Design*, vol. 14, pp. 1459-1469, Dec. 1995.

[11] C. G. Xu, "EPIC: A program for extraction of the resistance and capacitance of substrate with the Greens Function method," Department of ECE, Oregon State University, 2002.

[12] D. Ozis, T. Fiez, and K. Mayaram, "A comprehensive geometry-dependent macromodel for substrate noise coupling in heavily doped CMOS processes," *Proceedings of IEEE Custom Integrated Circuits Conference*, May 2002, pp. 497-500.

[13] A. Sharma, "Predictive methodologies for substrate parasitic extraction and modeling in heavily doped CMOS substrates," M.S. Thesis, Oregon State University, 2003.

[14] D. Ozis, "An efficient modeling approach for substrate noise coupling analysis with multiple contacts in heavily doped CMOS processes," M.S. Thesis, Oregon State University, August 2001.

[15] MEDICI Two-dimensional device simulation program, Version 2000.2.0, Avant! Corporation and Technology Modeling Associates, Inc., 2000.

[16] TAURUS Process and device modeling program, Version 2001.4.0, Avant! Corporation and Technology Modeling Associates, Inc., 2001.

[17] B. W. McGauphy, J. C. Chen, D. Sylvester and C. Hu, "A simple method for on-chip, sub-femto farad interconnect capacitance measurement," *IEEE Electrion Device Letters*, vol. 18, pp. 21-23, January 1997.

[18] R. Suravarapu, "Layout dependent and bias independent scalable substrate model for RF MOSFETs," M.S. Thesis, Oregon State University, 2003.

[19] E. Charbon, R. Gharpurey, R.G. Meyer, and A. Sangiovanni-Vincentelli, "Susbstrate optimization based on semi-analytical techniques," *IEEE Trans. Computer-Aided Design*, vol. 18, pp. 305-315, April 1998.

[20] B. R. Stanisic, N. K. Verghese, R. A. Rutenbar, R. L. Carley, and D. J. Allstot, "Addressing substrate coupling in mixed-mode IC's and power distribution synthesis," *IEEE J. Solid-State Circuits*, vol. 29, pp. 226-237, March 1994.

APPENDICES

APPENDIX A. PARAMETER EXTRACTION FLOW FOR THE N-P MODEL

The new N-P model is described by this equation.

$$\begin{cases} Virtual\_Separation = (\alpha_1 (N^+_{area})^{\alpha_2} + \alpha_3) Actual\_Separation + \beta_1 (N^+_{area})^{\beta_2} \\ Virtual\_Separation \geq Actual\_Separation \end{cases}$$

Parameters to extract: α_1, α_2, α_3, β_1, and β_2

Parameter Extraction Steps:

- Step 1: Obtain a calibrated doping profile of the substrate process as described in [13].
- Step 2: Obtain 6 data points of R_{12NP} from 6 N-P test structures. (simulations or measurements).
  - These test structures should include at least 2 different separations. For example, a minimum spacing between the N+-P+ contacts guided by the design rules (2μm for the technology used in this work) and a spacing of 4μm.
  - These test structures should include at least 3 different N+ contact sizes, such as 25μm x 1μm, 50μm x 1μm, and 200μm x 1μm.

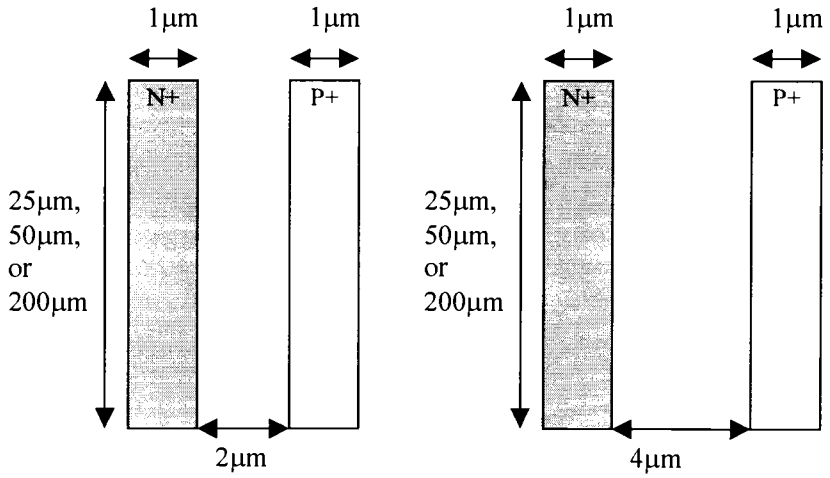

- Step 3: Simulate each structure in EPIC with the obtained calibrated profile.

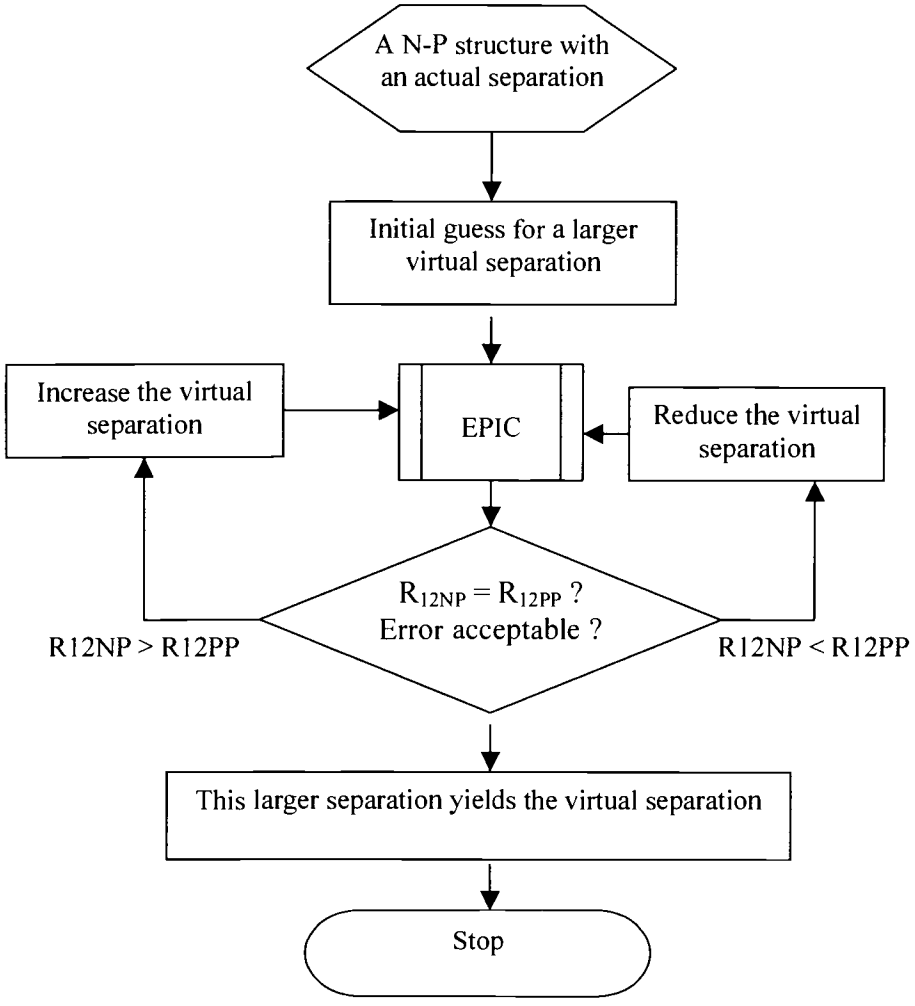

- Step 4: Plot the virtual separation versus the actual separation. With the structures provided in Step 2, *three* lines should be generated in this plot.

- Step 5: Curve fit α
  - Use the slopes of those *three* lines obtained in Step 4 and a slope of 1 for an extremely small N+ contact to curve fit α_1, α_2, and α_3 with this equation. α should approach to 1 as N+ contact size reduces.

$$\alpha = \alpha_1 (N^+_{area})^{\alpha_2} + \alpha_3$$

- Step 6: Curve fit β
  - Use any *two* of the y-intercepts of those curves obtained in Step 4 and a y-intercept of 0 for an extremely small N+ contact to curve fit β_1 and β_2 with this equation. β should approach to 0 as N+ contact size reduces.

$$\beta = \beta_1 (N^+_{area})^{\beta_2}$$

APPENDIX B. RESISTOR VALUES FOR COMPUTING THE RESISTANCE FOR FOUR-FINGER STRUCTURES

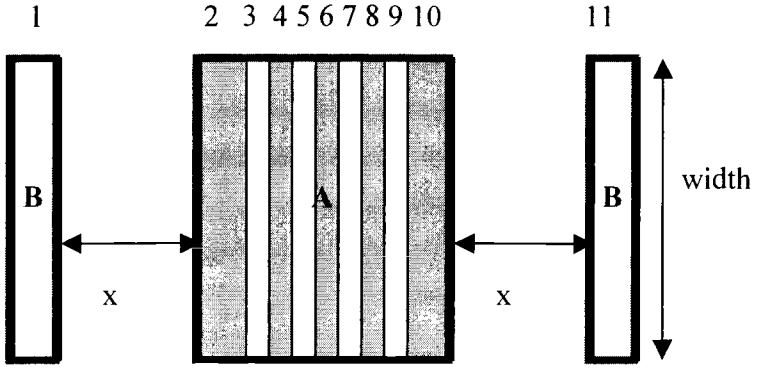

Figure B-1 4-finger structure. The shaded areas are the N+ contacts and the white areas are the P+ contacts. The width is 25μm and x is 2μm.

Figure B-1 shows a 4-finger structure with N+ contacts as shaded regions and P+ contacts as white regions. Contacts 2 to 10 are connected as node A and contacts 1 and 11 are connected as node B. The resistance is measured between nodes A and B. To apply the new N-P model, virtual separations are considered between contacts 1 and 2, contacts 1 and 4, contacts 8 and 11, and contacts 10 and 11. According to the N-P model, R_{12} and $R_{10\text{-}11}$ are obtained from the 4-finger structure with x equal to 3.4μm. The virtual separation between contacts 1 and 4 is computed as 4.05μm. After subtracting the length of contact 2 (1μm) and the length of contact 3 (0.6μm), the virtual distance of x is 2.45μm. Hence, R_{14} is computed from the 4-finger structure with x equal to 2.45μm. $R_{8\text{-}11}$ can be obtained from the

same structure. The resistance values of the substrate network between nodes A and B are summarized in Table B-1.

Table B-1 Resistive substrate network for the 4-finger structure with x = 2μm computed by the N-P model. The numbers in bold are the values computed with the new N-P model.

	(Ω)		(Ω)
R_{11}	6.502058e+02	R_{13}	3.801755e+03
R_{22}	2.145126e+03	R_{16}	2.842696e+04
R_{33}	7.401227e+03	R_{15}	6.855759e+04
R_{44}	3.754481e+03	$R_{9\text{-}11}$	2.955572e+03
R_{55}	1.098070e+04	$R_{6\text{-}11}$	3.615749e+04
R_{66}	4.422565e+03	$R_{7\text{-}11}$	3.230685e+04
R_{77}	6.916998e+03	**R_{14}**	**5.759019e+03**
R_{88}	3.490755e+03	**$R_{8\text{-}11}$**	**6.557548e+03**
R_{99}	6.091873e+03	**R_{12}**	**5.685057e+02**
$R_{10\text{-}10}$	2.298905e+03	**$R_{10\text{-}11}$**	**5.614110e+02**
$R_{11\text{-}11}$	6.424760e+02		

When x is equal to 5μm, 8μm, or 12μm, the virtual separation is equal to the actual separation. Hence, the resistance values of the substrate network are obtained directly from the 4-finger structure for these cases and are summarized in Table B-2, Table B-3, and Table B-4, respectively.

Table B-2 Resistive substrate network for the 4-finger structure with x = 5μm computed by the N-P model.

	P-model Value (Ω)		P-model Value (Ω)
R_{11}	5.413494e+02	R_{13}	8.018553e+03
R_{22}	1.560285e+03	R_{16}	4.484169e+04
R_{33}	6.668938e+03	R_{15}	1.235875e+05
R_{44}	3.648405e+03	$R_{9\text{-}11}$	6.433539e+03
R_{55}	1.097436e+04	$R_{6\text{-}11}$	5.639705e+04
R_{66}	4.436119e+03	$R_{7\text{-}11}$	5.449686e+04
R_{77}	6.926500e+03	R_{14}	9.792762e+03
R_{88}	3.416978e+03	$R_{8\text{-}11}$	1.087066e+04
R_{99}	5.491131e+03	R_{12}	8.071759e+02
$R_{10\text{-}10}$	1.624783e+03	$R_{10\text{-}11}$	7.724422e+02
$R_{11\text{-}11}$	5.351489e+02		

Table B-3 Resistive substrate network for the 4-finger structure with x = 8μm computed by the N-P model.

	P-model Value (Ω)		P-model Value (Ω)
R_{11}	4.823167e+02	R_{13}	1.335610e+04
R_{22}	1.244537e+03	R_{16}	6.627848e+04
R_{33}	6.029651e+03	R_{15}	1.628469e+05
R_{44}	3.486810e+03	$R_{9\text{-}11}$	9.356623e+03
R_{55}	1.090586e+04	$R_{6\text{-}11}$	7.349162e+04
R_{66}	4.378435e+03	$R_{7\text{-}11}$	7.312478e+04
R_{77}	6.847361e+03	R_{14}	1.591961e+04
R_{88}	3.323264e+03	$R_{8\text{-}11}$	1.535434e+04
R_{99}	5.091170e+03	R_{12}	1.370243e+03
$R_{10\text{-}10}$	1.355712e+03	$R_{10\text{-}11}$	1.139378e+03
$R_{11\text{-}11}$	5.025123e+02		

Table B-4 Resistive substrate network for the 4-finger structure with x = 12μm computed by the N-P model.

	P-model Value (Ω)		P-model Value (Ω)
R_{11}	4.273516e+02	R_{13}	2.281666e+04
R_{22}	1.036879e+03	R_{16}	1.005904e+05
R_{33}	5.486511e+03	R_{15}	2.469177e+05
R_{44}	3.325873e+03	$R_{9\text{-}11}$	1.909691e+04
R_{55}	1.069402e+04	$R_{6\text{-}11}$	1.235046e+05
R_{66}	4.287186e+03	$R_{7\text{-}11}$	1.323798e+05
R_{77}	6.676619e+03	R_{14}	2.640559e+04
R_{88}	3.155752e+03	$R_{8\text{-}11}$	2.980240e+04
R_{99}	4.490287e+03	R_{12}	2.381525e+03
$R_{10\text{-}10}$	1.046316e+03	$R_{10\text{-}11}$	2.380434e+03
$R_{11\text{-}11}$	4.356827e+02		